Pan-African Tectonism in the Western Maud Belt: *P–T–t* Path for High-grade Gneisses in the H.U. Sverdrupfjella, East Antarctica

W. S. BOARD[1], H. E. FRIMMEL[1]* AND R. A. ARMSTRONG[2]

[1]DEPARTMENT OF GEOLOGICAL SCIENCES, UNIVERSITY OF CAPE TOWN, RONDEBOSCH 7701, SOUTH AFRICA

[2]RESEARCH SCHOOL OF EARTH SCIENCES, AUSTRALIAN NATIONAL UNIVERSITY, CANBERRA, A.C.T. 002, AUSTRALIA

Extensive high-grade polydeformed metamorphic provinces surrounding Archaean cratonic nuclei in the East Antarctic Shield record two tectono-thermal episodes in late Mesoproterozoic and late Neoproterozoic–Cambrian times. In Western Dronning Maud Land, the high-grade Mesoproterozoic Maud Belt is juxtaposed against the Archaean Grunehogna Province and has traditionally been interpreted as a Grenvillian mobile belt that was thermally overprinted during the Early Palaeozoic. Integration of new U–Pb sensitive high-resolution ion microprobe and conventional single zircon and monazite age data, and Ar–Ar data on hornblende and biotite, with thermobarometric calculations on rocks from the H.U. Sverdrupfjella, northern Maud Belt, resulted in a more complex P–T–t evolution than previously assumed. A c. 540 Ma monazite, hosted by an upper ampibolite-facies mineral assemblage defining a regionally dominant top-to-NW shear fabric, provides strong evidence for the penetrative deformation in the area being of Pan-African age and not of Grenvillian age as previously reported. Relics of an eclogite-facies garnet–omphacite assemblage within strain-protected mafic boudins indicate that the peak metamorphic conditions recorded by most rocks in the area (T = 687–758°C, P = 9·4–11·3 kbar) were attained subsequent to decompression from P >12·9 kbar. By analogy with limited U–Pb single zircon age data and on circumstantial textural grounds, this earlier eclogite-facies metamorphism is ascribed to subduction and accretion around 565 Ma. Post-peak metamorphic K-metasomatism under amphibolite-facies conditions is ascribed to the intrusion of post-orogenic granite at c. 480 Ma. The recognition of extensive Pan-African tectonism in the Maud Belt casts doubts on previous Rodinia reconstructions, in which this belt takes a pivotal position between East Antarctica, the Kalahari Craton and Laurentia. Evidence of late Mesoproterozoic high-grade metamorphism during the formation of the Maud Belt exists in the form of c. 1035 Ma zircon overgrowths that are probably related to relics of granulite-facies metamorphism recorded from other parts of the Maud Belt. The polymetamorphic rocks are largely derived from a c. 1140 Ma volcanic arc and 1072 ± 10 Ma granite.

INTRODUCTION

The East Antarctic Shield consists of a series of Archaean nuclei surrounded by polydeformed Proterozoic metamorphic terrains of complex tectono-thermal history (Krynauw, 1996; Fitzsimons, 2000*b*). Radiometric age data clustering between 1300 and 900 Ma (traditionally compared with the 'Grenvillian' of North America) and between 600 and 450 Ma (the 'Pan-African' of Africa) have been reported from these polymetamorphic terrains throughout East Antarctica (Fitzsimons, 2000*b*, and references therein). The widespread occurrence of the former age group was interpreted as evidence of a continuous Grenville-age mobile belt. This so-called Circum East Antarctic Mobile Belt was linked with the Grenville Belt of North America and the resulting global-scale orogen considered the main suture in Rodinia reconstructions (Hoffman, 1991; Moores, 1991). Work in the Lützow–Holm Bay area (Shiraishi *et al.*, 1994), the Larsemann Hills (Dirks *et al.*, 1993), the Prydz Bay area (Fitzsimons *et al.*, 1997) and in parts of central Dronning Maud Land (Jacobs *et al.*, 1998, 2003), however, has led

*Corresponding author. Present address: Institute of Mineralogy and Petrology, University of Würzburg, Am Hubland, D-97074 Würzburg, Germany. Telephone: +49-931-888-5420. Fax: +49-931-888-4620. E-mail: Hartwig.Frimmel@mail.uni-wuerzburg.de
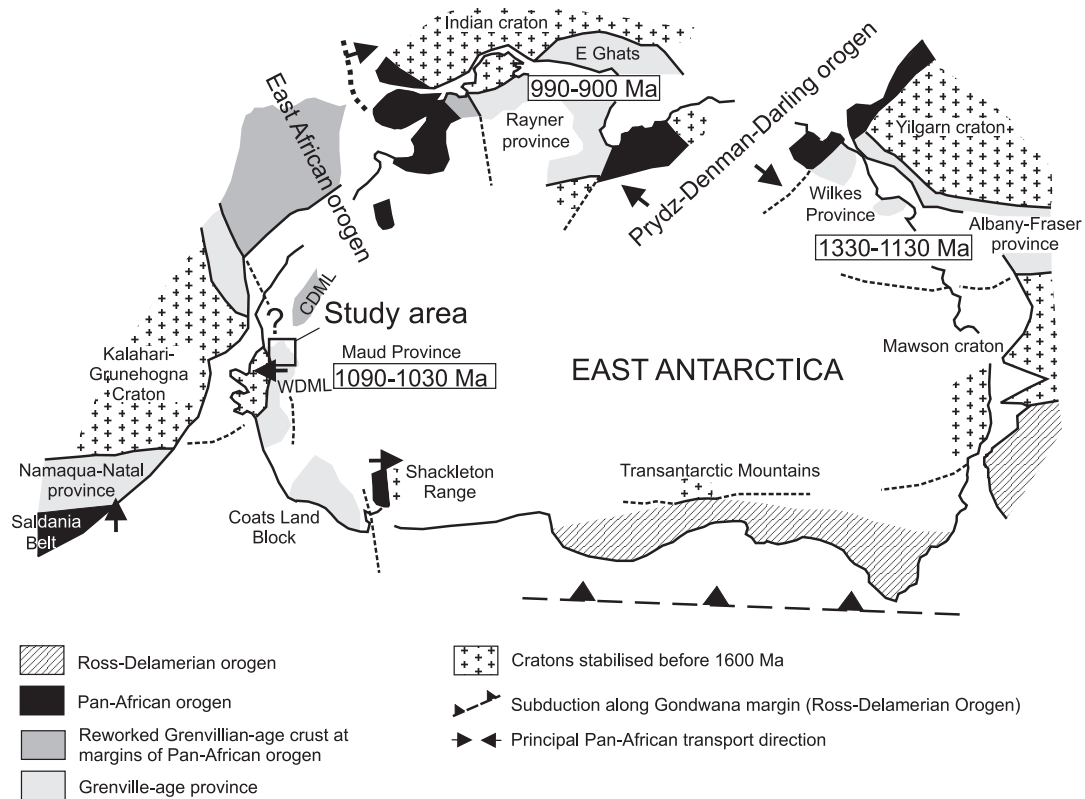
Fig. 1. Reconstruction of East Antarctica and adjacent parts of Gondwana at *c.* 500 Ma showing the distribution of Grenvillian and Pan-African tectonic domains [modified after Fitzsimons (2000*a*)]; CDML, Central Dronning Maud Land; WDML, Western Dronning Maud Land (study area).

to the recognition that Pan-African tectonic overprinting in East Antarctica is of a greater intensity and importance than was previously thought, thus challenging the hypothesis of a single continuous Grenville-age mobile belt around East Antarctica (Fitzsimons, 2000*a*).

Two main Pan-African orogenic belt systems have been recognized in East Antarctica (Fig. 1). The Prydz Belt is considered to extend from the Leeuwin Complex in Western Australia to Prydz Bay and then inland (Boger *et al.*, 2001), whereas the Lützow–Holm Belt (Fitzsimons, 2000*b*) is regarded as an extension of the East African Orogen into East Antarctica, where it passes through Lützow–Holm Bay and central Dronning Maud Land (Shiraishi *et al.*, 1994; Grunow *et al.*, 1996; Shackleton, 1996; Jacobs *et al.*, 1998). The role of the high-grade metamorphic rocks that make up the Maud Belt of western Dronning Maud Land in the tectonic evolution of East Antarctica remains elusive.

Both a thermal and a tectono-thermal model have been proposed for the Pan-African history of the Maud Belt. In the former, the belt is considered a Grenville-age orogenic belt that experienced purely thermal overprinting during Pan-African times (Groenewald *et al.*, 1995), whereas, in the latter, considerable orogenic deformation is assumed to have taken place during Pan-African times (Jacobs *et al.*, 1998, 1999, 2003). Clarification of this issue is pivotal for any attempt to reconstruct the palaeogeography during assembly and break-up of an inferred Mesoproterozoic supercontinent (be it Rodinia or any other configuration) and subsequent amalgamation of Gondwana.

Evidence of a purely thermal, Pan-African overprint stems largely from the central to northeastern Maud Belt, i.e. the nunataks of Kirwanveggen and H.U. Sverdrup-fjella (Fig. 2), where the penetrative fabric, resulting from top-to-NW thrusting, has been interpreted as Grenvillian in age (Grantham *et al.*, 1995; Groenewald *et al.*, 1995). In contrast, strong evidence for Pan-African tectonic activity has been provided for the southwestern part of the belt by Golynsky & Jacobs (2001), who argued on structural and aeromagnetic grounds for a major shear zone there (Heimefront Shear Zone, Fig. 2) to be the continuation of the East African orogenic front.

The aim of this study is to examine the age of the penetrative fabric in the northern portion of the Maud Belt, specifically in southern parts of the eastern H.U. Sverdrupfjella, where the best exposed and most complete cross-section through the tectonostratigraphic units
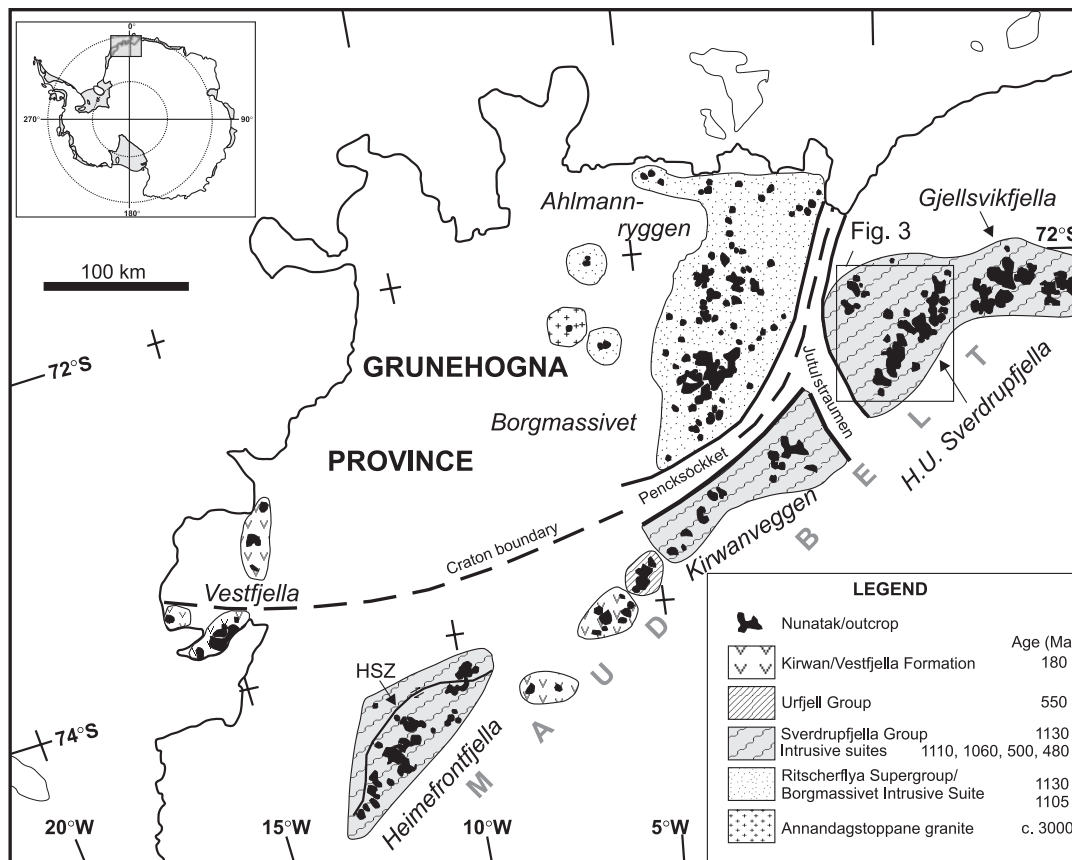
Fig. 2. Geological map of western Dronning Maud Land, Antarctica; HSZ–Heimefront Shear Zone.

of the northern Maud Belt can be found. To that effect, new sensitive high-resolution ion microprobe (SHRIMP) and conventional U–Pb single zircon and monazite ages as well as Ar–Ar ages on hornblende and biotite are presented, together with detailed petrography and geothermobarometry, to generate a pressure–temperature–time (*P–T–t*) path for the high-grade gneisses in that area.

GEOLOGICAL SETTING

Western Dronning Maud Land extends from ∼70°S to ∼75°S and from ∼15°W to ∼03°E. It consists of two geological provinces: the Archaean to Mesoproterozoic Grunehogna Province and the Mesoproterozoic to early Palaeozoic Maud Belt (Krynauw, 1996). The Grunehogna Province, which is interpreted as a portion of the Kalahari Craton that became detached during Gondwana break-up, is assumed to be in tectonic juxtaposition with the Maud Belt along an inferred crustal discontinuity that is masked by the Pencksökket and lower Jutulstraumen glaciers (Fig. 2).

In the mountain range and isolated nunataks of H.U. Sverdrupfjella (Fig. 3), the structurally lowest exposed

unit consists of intercalated tonalitic orthogneiss and hornblende–biotite gneiss (Jutulrøra Formation). It is interpreted as a volcanic arc sequence of interlayered calc-alkaline volcanic and clastic sedimentary rocks on the basis of geochemical and field characteristics (Groenewald *et al.*, 1995). This is followed by a sequence of compositionally banded, in places migmatitic, biotite–hornblende gneiss with highly variable proportion of felsic and mafic minerals and dominance of plagioclase over K-feldspar, and intercalated discontinuous, boudinaged lenses of calcitic marble, calc-silicate, and amphibolite, all of which constitutes the Fuglefjellet Formation (Fig. 4).

Semipelitic garnet–biotite gneiss, quartzofeldspathic paragneiss and intermediate to felsic orthogneiss with subordinate amphibolite and calc-silicate enclaves (Rootshorga Formation) dominate the outcrops along the entire length of the eastern H.U. Sverdrupfjella. The banded nature and conformity with the layering in the paragneiss points to a volcanic rather than plutonic origin of the orthogneiss units. Although previous workers (Grantham *et al.*, 1995; Groenewald *et al.*, 1995) inferred a tectonic contact between the Fuglefjellet and Rootshorga Formations, fieldwork by the authors
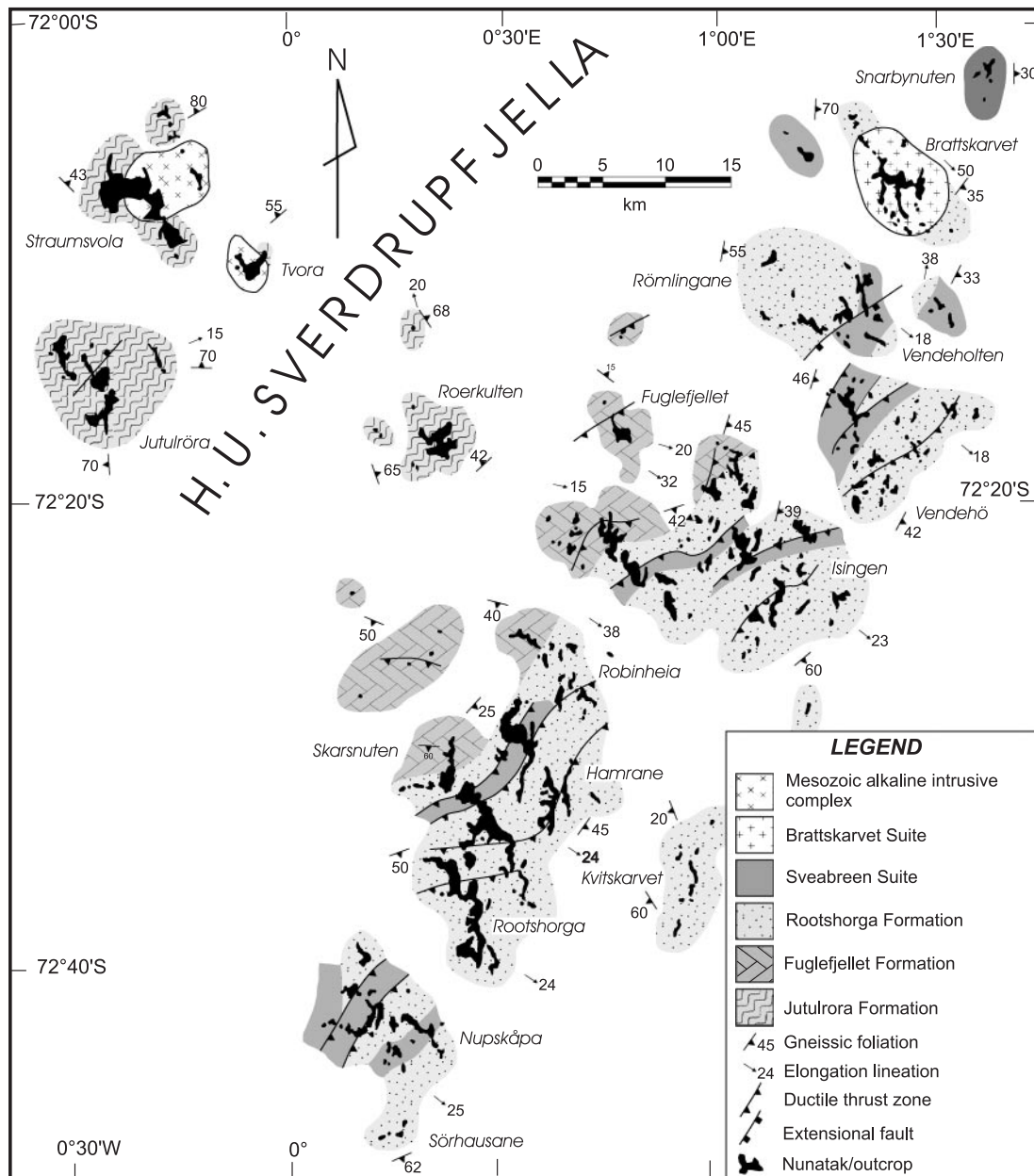
Fig. 3. Tectono-stratigraphic map of the H.U. Sverdrupfjella [modified after Groenewald *et al.* (1995)].

revealed a gradational transition from the former to the latter formation in a low-strain zone NE of Skarsnuten (Fig. 3). This transition is characterized by an increase in the biotite/hornblende ratio within the paragneiss and a decrease in the amount of carbonate and calc-silicate intercalations.

A retroarc basin is envisaged for the depositional environment of the Fuglefjellet and Rootshorga Formations on the basis of their respective field relationships and geochemistry (Groenewald *et al.*, 1995; Board, 2002). A Rb–Sr whole-rock age of 1145 ± 49 Ma for a

metavolcanic unit within the banded gneisses of the Jutulrøra Formation (A. Moyes, unpublished data, 1986), a U–Pb SHRIMP zircon age of 1131 ± 25 Ma (Harris *et al.*, 1995) for a sample of pre-tectonic garnet–biotite granitic gneiss of calc-alkaline composition, and a U–Pb single zircon age of 1131 ± 7 Ma for a related felsic tuff layer in the corresponding foreland deposits of the Ritscherflya Supergroup (Frimmel, 2004) constrain the age of the volcanic island arc.

Slightly younger (1103 ± 17 Ma; Harris *et al.*, 1995) deformed tabular, in places distinctly megacrystic,
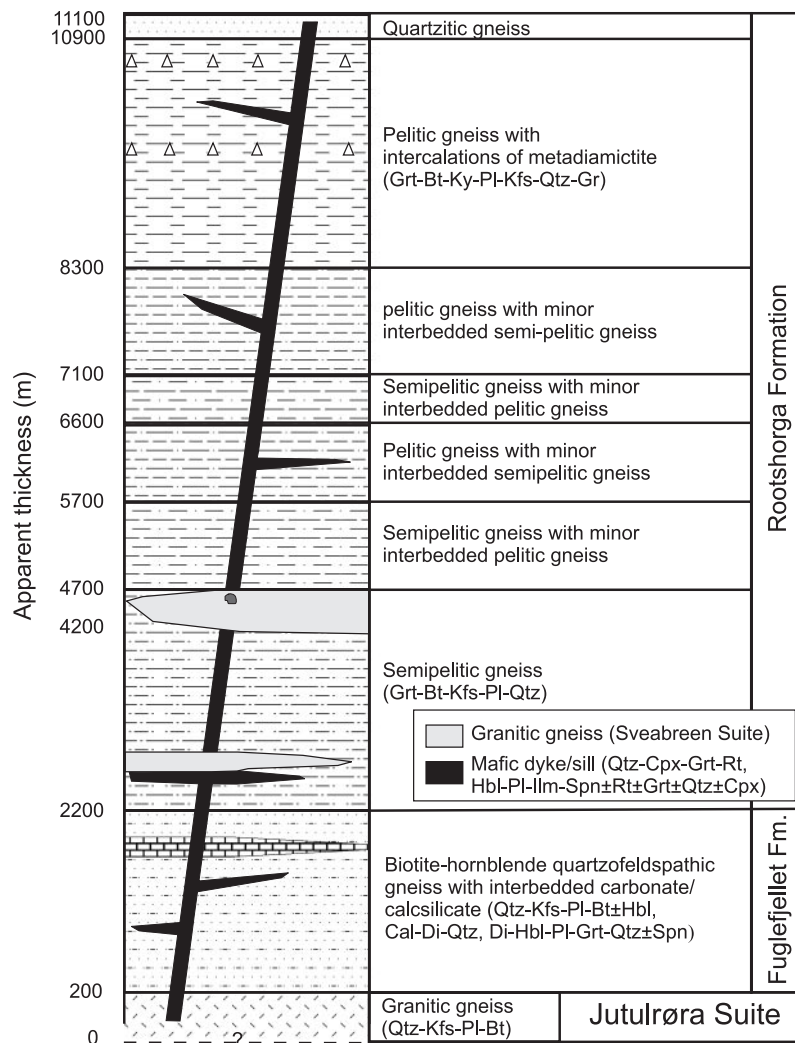
Fig. 4. Schematic lithostratigraphic profile for the northern Maud Belt in southern H.U. Sverdrupfjella [mineral abbreviations after Kretz (1983)].

granite gneiss bodies (Sveabreen Suite) display a within-plate geochemical affinity (Groenewald *et al.*, 1995; Board, 2002). Several generations of deformed mafic intrusions are distinguished. The majority of the mafic bodies occur as lenses, boudins, concordant layers (sills or lava flows) and rarely dykes. They pre-date the deformation and are intrusive into the oldest pre-tectonic granite.

Post-tectonic plutons, sheets and dykes of monzogranitic composition (Brattskarvet Suite) are widespread. Mesozoic alkaline complexes (170 ± 4 Ma) and undeformed Jurassic dolerite dykes (Grantham *et al.*, 1988; Harris & Grantham, 1993) are related to the break-up of Gondwana and reflect the youngest magmatic pulse in the area.

Five phases of deformation (D_1–D_5) have been recognized (Grantham *et al.*, 1995). Transposition of earlier structures is evident in the presence of numerous rootless intrafolial folds, ascribed to D_1. The penetrative fabric (S_2) is shallow east-dipping (in the western domain) to moderately SE-dipping (in the eastern domain) and related to east- to SE-plunging tight to isoclinal folds and sheath folds, a moderately east- to SE-plunging mineral elongation lineation, and dominant top-to-NW shear sense (D_2). The orientation of the majority of fold axes corresponds very closely to that of the mineral elongation lineations and the fold axes determined from foliation data. Regional warping and local NE–SW-trending open folds, in places leading to a top-to-SE reverse shear sense, reoriented the S_2 fabric slightly and led to localized fabric transposition defined by biotite (D_3). Localized large-scale open, upright folding on NE-trending axes reflect D_4 in the western and northeastern parts of the H.U. Sverdrupfjella, whereas in the southern domain, regional-scale gentle warping of the SE-dipping

S_2 fabric and D_2 high-strain zones about moderately SE-plunging axes mark D_4. The development of steep to vertical normal faults and joints with north–south and NE–SW trends is the youngest deformation recognized in the H.U. Sverdrupfjella (D_5).

Both D_1 and D_2 have been assigned a Grenvillian age by Grantham *et al.* (1995) based on the assumption that the Sveabreen granitic gneiss was emplaced post-D_1 and syntectonically with respect to D_2. Localized fabric development within the Brattskarvet Suite has led some of those workers to interpret D_3 and D_4 as Pan-African in age. However, a magmatic origin of the rather chaotic and multi-directional structures in the Brattkarvet pluton is considered more likely. The similarity in the orientation of the stress fields for the D_1 to D_4 deformations makes a clear distinction difficult in many places and their age remains uncertain. There is general agreement that the youngest deformation, D_5, is related to the Mesozoic break-up of Gondwana (Groenewald *et al.*, 1995).

The metamorphic history of the area is complex. Evidence of the earliest stage of metamorphism (M_1) comes from cores of pre-tectonic mafic boudins that display a granulite-facies mineral assemblage for which P–T conditions of 8–10 kbar and 850°C have been estimated (Groenewald & Hunter, 1991). The majority of the rock types throughout the H.U. Sverdrupfjella consist of syn-kinematic (syn-D_2) mineral assemblages characteristic of the upper amphibolite facies (Fig. 4). Metapelitic gneisses show abundant evidence of partial melting with pre-, syn- and post-tectonic leucosome domains. In contrast, no evidence of partial melting exists within the mafic rocks. In the eastern area, Grantham *et al.* (1995) distinguished an early high-pressure stage (P = 9–20 kbar; T = 720–850°C) from a subsequent near-isothermal decompression to conditions transitional between amphibolite and granulite (P = 5–8 kbar; T = 600–790°C), retrograde rehydration at similar P–T conditions, all of which constitute M_2, and localized late-stage greenschist-facies conditions (M_3). Evidence of the latter is confined to syn-D_5 fractures and joints and the wall rock of undeformed dolerite dykes.

In the western area, the distinction between the various metamorphic events is problematic, as only amphibolite-facies conditions (P = 3–9 kbar; T = 620–700°C) have been described (Grantham *et al.*, 1995). Some of the above P–T constraints are rather loose and problematic, because of the use of unreliable geothermobarometers and potential disequilibrium among the mineral assemblages used, but a recent re-examination of the metamorphic conditions recorded by amphibolites there indicated peak temperatures around 730°C (Grosch & Frimmel, 2004). Grantham *et al.* (1995) interpreted the apparent differences in structural style and metamorphic evolution between the western and eastern H.U. Sverdrupfjella as indicating that the rocks of the latter were thrust over those of the former during D_2, but the more recent results (Grosch & Frimmel, 2004) do not support this.

PETROGRAPHY AND MINERAL CHEMISTRY

Mineral assemblages in the felsic gneiss, semi-pelitic gneiss, carbonate and calc-silicate units (Fig. 4) provide only limited constraints on the metamorphic history. However, mineral assemblages and disequilibrium textures developed in the cores of competent anhydrous metabasic rocks, which form resistant tectonic lenses and boudins, and in the metapelitic rocks are more useful to place constraints on the P–T evolution of the area. Six amphibolite samples, representing the range of mafic rock types in the southern H.U. Sverdrupfjella, and three samples of metapelitic gneiss were therefore chosen for mineral chemical analysis. The mineral chemical data (Electronic Appendix 1, which may be downloaded from the *Journal of Petrology* website at http://www.petrology.oupjournals.org) were acquired by conventional electron microprobe analysis using a Cameca Camebax instrument at the Department of Geological Sciences, University of Cape Town. The instrument was run at an accelerating voltage of 15 kV [25 kV for the analysis of rare earth elements (REE) in monazite] and a beam current of ∼40 nA. Counting times at peak and background positions were 10 s, with the beam defocused to ∼2–3 μm. Natural and synthetic standards were used for calibration and the Cameca PAP correction procedure was employed. The detection limits for the elements analysed for are between 0·02 and 0·09%. Mineral abbreviations used are from Kretz (1983). All Fe is expressed as Fe^{2+} unless otherwise stated.

Metabasic rocks

The oldest mineral assemblage recorded within the cores of some of the pre-tectonic mafic rocks is Grt–Cpx–Qtz–Rt. Little of the original assemblage is preserved, however, because of the extensive re-equilibration of these rocks during subsequent metamorphism that led to the widespread development of the assemblage Hbl–Pl–Ilm–Spn. In most of the pre-tectonic mafic rocks, the presence of garnet and clinopyroxene is mainly inferred from the occurrence of pseudomorphs of plagioclase and hornblende. However, earlier garnet and, very rarely, clinopyroxene are still preserved in cores of resistant tectonic lenses. That garnet occurs as sub-rounded to irregularly shaped grains (1–4 mm in size), contains inclusions of rutile and quartz, and is commonly surrounded by a symplectitic corona of hornblende and plagioclase (Fig. 5b). Clinopyroxene occurs as irregularly shaped
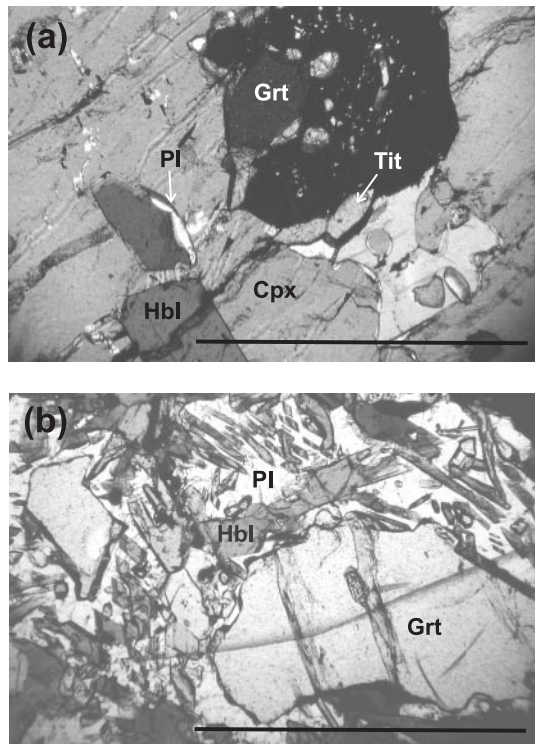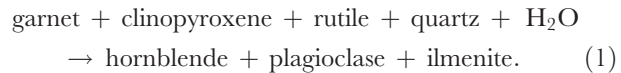
Fig. 5. (a) Garnet (Grt), clinopyroxene (Cpx) and titanite (Tit) with only limited hydration to syn-M_2 hornblende (Hbl), sample WBSV079, crossed polars. (b) Relic garnet surrounded by symplectitic hornblende and plagioclase (Pl), sample WBSV034, parallel polars. Scale bars represent 1 mm.

grains (>3 mm in length) that are generally separated from the garnet and the matrix by a rim of either hornblende or hornblende–plagioclase symplectite. Plagioclase exsolution lamellae constitute up to ~45 vol. % of the clinopyroxene grains, and small patches of hornblende occur in places, formed at the expense of clinopyroxene. In one sample (WBSV079), however, granoblastic clinopyroxene relics that are free of plagioclase exsolution lamellae appear to be in textural equilibrium with garnet, hornblende and plagioclase (Fig. 5a).

Most amphibolite samples are dominated by hornblende and plagioclase. These minerals typically form symplectitic intergrowths where they surround relics of the older Grt–Cpx assemblage (Fig. 5b), and have a granoblastic texture where they occur as matrix minerals. The presence of symplectitic intergrowths and clinopyroxene grains with plagioclase exsolution lamellae suggests limited fluid infiltration into the core of those metabasic rocks in which such textures are preserved. Rutile and ilmenite, in places rimmed by titanite, occur both within the matrix and as inclusions within hornblende. Titanite is in textural equilibrium with the hornblende and plagioclase, which define a fabric in the foliated outer portions of the pre-tectonic metabasic boudins that corresponds to the regional S_2.

The above textures suggest decompression from eclogite-facies to upper amphibolite-facies conditions by the continuous reaction

$$\text{garnet} + \text{clinopyroxene} + \text{rutile} + \text{quartz} + \text{H}_2\text{O}$$
$$\rightarrow \text{hornblende} + \text{plagioclase} + \text{ilmenite}. \quad (1)$$

The large proportion of plagioclase exsolution lamellae in the clinopyroxene is a typical feature of decompressed eclogites (Boland & van Roermund, 1983) and indicates a precursor of omphacitic composition that expelled jadeite and tschermakite components by the reaction

$$\text{sodic clinopyroxene} + \text{quartz}$$
$$\rightarrow \text{calcic clinopyroxene} + \text{plagioclase}. \quad (2)$$
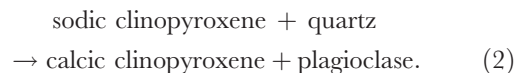
The absence of a penetrative fabric associated with the Grt–Cpx assemblage suggests a pre-tectonic (pre-D_2) origin for this assemblage, although this could simply be due to the competent nature of the mafic bodies, making such rocks generally more resistant to deformation than the host paragneiss. The good preservation of the decompression textures described above points to the eclogite- and amphibolite-facies assemblages having formed during the same tectonic episode, whereby metamorphic recrystallization outlasted deformation (D_2).

Widely spaced biotite laths cut across the above mineral assemblages. The abundance of biotite laths generally increases from the cores (≪1 vol. %) to the edges (up to 20 vol. %) of the mafic bodies, although the cores of many of the more re-equilibrated rocks contain up to 15 vol. % biotite. This distribution is consistent with biotite formation being related to potassic fluid infiltration during a retrograde metamorphic stage. Although some of the biotite grains are aligned parallel to S_2, most are randomly oriented. Both textural types of biotite have the same composition. The metabasic rocks do not display an S_3 fabric, and the latest metamorphic imprint recognized is the local replacement of biotite by chlorite near syn-D_5 fractures and joints.

A total of 476 electron microprobe analyses were obtained of garnet, clinopyroxene, plagioclase, ilmenite, amphibole and biotite. Representative mineral analyses for each sample are given in Tables 1 and 2. The complete dataset may be downloaded from the *Journal of Petrology* website at http://www.petrology.oupjournals.org/ (Electronic Appendix 1).

Garnet is present (10–55 vol. %) in all of the metabasic samples analysed and consists predominantly of almandine ($X_{\text{Alm}} = 46–62\%$, $X_{\text{Gro}} = 17–31\%$, $X_{\text{Pyr}} = 11–23\%$, $X_{\text{Sps}} = 0\cdot6–4\cdot3\%$). $X_{\text{Fe}} = \text{Fe}/(\text{Fe} + \text{Mg})$ values range from 0·67 to 0·84. Garnet is mostly homogeneous. In some grains, X_{Sps} displays a slight decrease with a corresponding increase in X_{Pyr} from core to rim, with X_{Gro} remaining constant.

Table 1: Representative electron microprobe analyses of garnet (Grt), plagioclase (Pl), Ilmenite (Ilm) and clinopyroxene (Cpx) for the samples of pre-tectonic metabasic rock

Sample:	WBSV031				WBSV034							WBSV041					WBSV066		WBSV079					
Locality:	72°32·800'S, 000°25·955'E				72°33·057'S, 000°26·018'E							72°33·284'S, 000°26·564'E					72°30·432'S, 000°22·891'E		72°36·276'S, 000°24·682'E					
Rock:	Grt amphibolite dyke				Cpx–Grt amphibolite boudin							Grt amphibolite boudin					Cpx–Grt amph		Cpx–Grt amphibolite boudin					
Grain no.:	Grt-7	Grt-3	Pl-6	Ilm-2	Grt-35	Grt-32	Pl-9	Pl-24	Pl-1	Ilm-6	Cpx-5	Grt-20	Grt-16	Pl-3	Pl-7	Ilm-1	Pl-4	Cpx-3	Grt-4	Grt-1	Pl-1	P-5	Ilm-1	Cpx-7
	core	rim			core	rim	smp.1	smp.2	exsoln.			core	rim	smp.1	smp.2				core	rim				
SiO$_2$	37·17	37·36	61·30	0·06	37·93	37·80	51·03	57·87	59·95	0·00	51·63	38·52	37·83	51·57	57·78	0·79	65·31	50·15	37·82	37·64	61·39	59·34	0·01	51·78
TiO$_2$	0·01	0·02	0·00	52·71	0·10	0·09	0·00	0·00	0·00	52·57	0·21	0·09	0·09	0·00	0·00	53·50	0·00	0·00	0·05	0·06	0·00	0·00	54·28	0·21
Al$_2$O$_3$	21·01	21·41	25·33	0·04	21·36	21·93	31·99	27·83	25·80	0·04	2·07	21·63	21·80	31·37	27·62	0·06	21·64	0·68	21·53	20·93	24·45	25·51	0·04	2·66
Cr$_2$O$_3$	0·00	0·00	0·00	0·00	0·03	0·04	0·00	0·00	0·00	0·01	0·02	0·00	0·00	0·00	0·00	0·00	0·00		0·00	0·04	0·00	0·00	0·00	0·03
FeO	26·26	27·24	0·08	46·76	24·94	25·68	0·18	0·10	0·09	46·43	9·81	22·72	23·54	0·26	0·23	45·23	0·01	16·49	27·00	25·27	0·07	0·15	44·87	10·27
MnO	1·10	1·38	0·00	0·87	0·87	0·33	0·00	0·00	0·00	0·49	0·07	0·40	0·41	0·00	0·00	0·75	0·00	0·49	1·22	0·58	0·00	0·00	0·27	0·10
MgO	3·89	4·08	0·00	0·45	5·21	6·11	0·02	0·00	0·01	0·62	12·95	5·76	5·24	0·01	0·01	0·25	0·00	8·49	3·18	3·87	0·01	0·02	1·22	12·46
CaO	9·51	8·27	5·67	0·01	9·63	8·90	12·98	7·86	6·25	0·01	22·02	11·25	10·94	12·88	8·13	0·00	2·56	22·42	10·18	10·73	6·18	7·41	0·12	22·59
Na$_2$O	0·13	0·09	7·38	0·00	0·08	0·05	4·00	5·63	8·15	0·00	0·35	0·06	0·04	4·19	6·16	0·03	9·23	0·46	0·01	0·03	7·55	6·81	0·00	0·43
K$_2$O	0·00	0·00	0·09	0·00	0·00	0·00	0·06	0·10	0·29	0·00	0·08	0·00	0·00	0·00	0·00	0·00	0·40	0·00	0·00	0·00	0·52	0·43	0·00	0·00
Total	99·08	99·85	99·84	100·88	100·15	100·94	100·26	99·39	100·53	100·17	99·21	100·43	99·89	100·28	99·93	100·60	99·14	99·17	100·97	99·14	100·16	99·66	100·82	100·53
Si	2·96	2·96	2·71	0·00	2·96	2·93	2·31	2·59	2·66	0·00	1·95	2·97	2·95	2·33	2·58	0·02	2·89	1·97	2·97	2·98	2·72	2·66	0·00	1·94
Ti	0·00	0·00	0·00	0·99	0·01	0·01	0·00	0·00	0·00	0·99	0·01	0·01	0·01	0·00	0·00	1·00	0·00	0·00	0·00	0·00	0·00	0·00	1·01	0·01
Al	1·97	2·00	1·32	0·00	1·97	2·00	1·71	1·47	1·35	0·00	0·09	1·97	2·00	1·67	1·45	0·00	1·13	0·03	1·99	1·96	1·28	1·35	0·00	0·12
Cr	0·00	0·00	0·00	0·00	0·00	0·00	0·00	0·00	0·00	0·00	0·00	0·00	0·00	0·00	0·00	0·00	0·00	0·00	0·00	0·00	0·00	0·00	0·00	0·00
Fe	1·75	1·80	0·00	0·98	1·63	1·66	0·01	0·00	0·00	0·98	0·31	1·47	1·53	0·01	0·01	0·94	0·00	0·54	1·77	1·68	0·00	0·01	0·93	0·32
Mn	0·07	0·09	0·00	0·02	0·06	0·02	0·00	0·00	0·00	0·01	0·00	0·03	0·03	0·00	0·00	0·02	0·00	0·02	0·08	0·04	0·00	0·00	0·01	0·00
Mg	0·46	0·48	0·00	0·02	0·61	0·70	0·00	0·00	0·00	0·02	0·73	0·66	0·61	0·00	0·00	0·01	0·00	0·50	0·37	0·46	0·00	0·00	0·04	0·69
Ca	0·81	0·70	0·27	0·00	0·81	0·74	0·63	0·38	0·30	0·00	0·89	0·93	0·91	0·62	0·39	0·00	0·12	0·94	0·85	0·91	0·29	0·36	0·00	0·90
Na	0·02	0·01	0·63	0·00	0·01	0·01	0·35	0·49	0·70	0·00	0·03	0·01	0·01	0·37	0·53	0·00	0·79	0·04	0·00	0·00	0·65	0·59	0·00	0·03
K	0·00	0·00	0·01	0·00	0·00	0·00	0·00	0·01	0·02	0·00	0·00	0·00	0·00	0·00	0·00	0·00	0·02	0·00	0·00	0·00	0·03	0·02	0·00	0·00
Total	8·06	8·05	4·95	2·01	8·05	8·07	5·01	4·93	5·03	2·01	4·01	8·04	8·05	5·01	4·96	1·98	4·95	4·03	8·04	8·03	4·98	4·98	1·99	4·01

smp.1, high-Ca plagioclase in symplectite; smp.2, 'intermediate-Ca' plagioclase in symplectite; exsoln., plagioclase exsolution lamellae in Cpx. Formulae calculated on the basis of 12 oxygens for garnet, eight for plagioclase, three for ilmenite and six for clinopyroxene. All Fe reported as FeO.

Table 2: Representative electron microprobe analyses of hornblende (Hbl) and biotite (Bt) for the samples of pre-tectonic metabasic rock

Oxides (wt %)

	31 Hbl-4	34 Hbl-23	41 Hbl-3	66 Hbl-14	79 Hbl-7	31 Bt-7	34 Bt-10	47 Bt-5 s	47 Bt-10 r	66 Bt-5	79 Bt-2
SiO_2	43·16	42·07	43·77	39·37	41·03	37·57	36·52	36·73	36·36	34·03	35·43
TiO_2	1·28	1·62	0·41	1·52	1·94	2·63	4·38	2·00	2·34	3·14	5·25
Al_2O_3	13·43	14·15	12·35	10·65	13·24	16·82	15·48	17·13	17·16	13·87	14·83
Cr_2O_3	0·05	0·05	0·03	0·04	0·05	0·01	0·00	0·00	0·00	0·00	0·00
FeO	16·95	16·06	18·62	23·84	15·27	18·62	17·89	21·87	22·55	26·34	18·71
MnO	0·24	0·10	0·20	0·37	0·06	0·07	0·00	0·29	0·33	0·23	0·07
MgO	10·26	9·71	8·96	6·03	10·12	12·60	12·97	7·80	7·80	7·43	11·49
CaO	10·99	11·55	11·50	11·28	11·66	0·03	0·03	0·00	0·00	0·03	0·02
Na_2O	1·43	1·46	1·04	1·74	1·38	0·33	0·24	0·07	0·08	0·11	0·14
K_2O	0·57	1·29	0·46	1·46	1·41	8·41	8·29	8·22	8·40	8·93	8·95
F						n.d.	0·63	0·86	0·76	0·42	n.d.
Total	98·37	98·06	97·33	96·31	96·16	97·11	96·42	94·98	95·78	94·53	94·88

Hornblende cation formulae

	Hbl-4 a	Hbl-4 b	Hbl-4 c	Hbl-23 a	Hbl-23 b	Hbl-23 c	Hbl-3 a	Hbl-3 b	Hbl-3 c	Hbl-14 a	Hbl-14 b	Hbl-14 c	Hbl-7 a	Hbl-7 b	Hbl-7 c
Si	6·39	6·32	6·26	6·27	6·24	6·21	6·59	6·52	6·48	6·29	6·23	6·22	6·25	6·22	6·20
Al^{IV}	1·61	1·68	1·74	1·73	1·76	1·79	1·41	1·48	1·52	1·71	1·77	1·78	1·75	1·78	1·80
T-Site	8·00	8·00	8·00	8·00	8·00	8·00	8·00	8·00	8·00	8·00	8·00	8·00	8·00	8·00	8·00
Al^{VI}	0·74	0·64	0·55	0·76	0·72	0·68	0·78	0·69	0·64	0·30	0·22	0·20	0·62	0·59	0·56
Ti	0·14	0·14	0·14	0·18	0·18	0·18	0·05	0·05	0·05	0·18	0·18	0·18	0·22	0·22	0·22
Fe^{3+}	0·00	0·53	0·98	0·00	0·21	0·42	0·00	0·48	0·74	0·00	0·44	0·58	0·01	0·18	0·35
Cr	0·01	0·01	0·01	0·01	0·01	0·01	0·00	0·00	0·00	0·01	0·01	0·01	0·01	0·01	0·01
Mg	2·27	2·24	2·22	2·16	2·15	2·14	2·01	1·99	1·98	1·44	1·42	1·42	2·30	2·29	2·28
Fe^{2+}	1·85	1·44	1·07	1·90	1·74	1·56	2·16	1·79	1·56	3·07	2·72	2·57	1·85	1·72	1·58
Mn	0·00	0·00	0·03	0·00	0·00	0·01	0·00	0·00	0·03	0·00	0·01	0·05	0·00	0·00	0·01
C-site	5·00	5·00	5·00	5·00	5·00	5·00	5·00	5·00	5·00	5·00	5·00	5·00	5·00	5·00	5·00
Mg	0·00	0·00	0·00	0·00	0·00	0·00	0·00	0·00	0·00	0·00	0·00	0·00	0·00	0·00	0·00
Fe^{2+}	0·25	0·10	0·00	0·11	0·05	0·00	0·19	0·05	0·00	0·12	0·00	0·00	0·09	0·04	0·00
Mn	0·03	0·03	0·00	0·01	0·01	0·00	0·03	0·03	0·00	0·05	0·04	0·00	0·01	0·01	0·00
Ca	1·72	1·72	1·71	1·85	1·84	1·83	1·79	1·84	1·83	1·83	1·91	1·91	1·90	1·89	1·89
Na	0·00	0·15	0·29	0·03	0·10	0·17	0·00	0·09	0·17	0·00	0·05	0·09	0·00	0·06	0·11
B-site	2·00	2·00	2·00	2·00	2·00	2·00	2·00	2·00	2·00	2·00	2·00	2·00	2·00	2·00	2·00
Ca	0·03	–		0·00	–		0·07	–		0·10	–		0·00	–	
Na	0·41	0·26	0·11	0·39	0·32	0·25	0·30	0·21	0·12	0·54	0·49	0·44	0·41	0·35	0·29
K	0·11	0·11	0·11	0·25	0·24	0·24	0·09	0·09	0·09	0·30	0·30	0·29	0·27	0·27	0·27
A-site	0·55	0·37	0·22	0·63	0·56	0·49	0·46	0·30	0·21	0·93	0·78	0·73	0·68	0·62	0·56
Total	15·55	15·37	15·22	15·63	15·56	15·49	15·46	15·30	15·21	15·93	15·78	15·73	15·68	15·62	15·56

Biotite cation formulae

	31 Bt-7	34 Bt-10	47 Bt-5 s	47 Bt-10 r	66 Bt-5	79 Bt-2
Si	6·05	5·93	6·14	6·06	5·96	5·92
Al^{IV}	1·95	2·07	1·86	1·94	2·04	2·08
T-Site	8·00	8·00	8·00	8·00	8·00	8·00
Al^{VI}	1·25	0·89	1·51	1·43	0·82	0·84
Ti	0·32	0·53	0·25	0·29	0·41	0·66
Cr	0·00	0·00	0·00	0·00	0·00	0·00
Fe^{2+}	2·51	2·43	3·06	3·14	3·86	2·61
Mn	0·01	0·00	0·04	0·05	0·03	0·01
Mg	3·03	3·14	1·94	1·94	1·94	2·86
O-site	7·11	6·99	6·81	6·85	7·06	6·98
Ca	0·01	0·01	0·00	0·00	0·01	0·00
Na	0·10	0·08	0·02	0·03	0·04	0·05
K	1·73	1·72	1·75	1·79	1·99	1·91
A-site	1·84	1·80	1·78	1·81	2·04	1·96
Total	16·95	16·79	16·58	16·66	17·10	16·94

Formulae based on 23 oxygens for hornblende and 24(O + OH) for biotite. All Fe reported as FeO. s, biotite parallel to S_2; r, randomly oriented biotite; n.d., not determined; a, formulae based on all Fe as Fe^{2+}; b,c, formulae based on average and maximum ferric iron estimates of Leake *et al.* (1997).

Clinopyroxene (up to 30 vol. %) is homogeneous and contains between 19·4 and 24·1 wt % CaO, with 2–7% jadeite, up to 9% calcium-tschermakite and up to 1% aegirine contents. X_{Fe} varies considerably between samples (0·26–0·53) but is relatively uniform within samples.

Plagioclase is present in variable proportions (5–35 vol. %) in all of the analysed samples. Individual grains are homogeneous, but up to three compositionally different varieties are present within a given sample. Their anorthite contents are $An_{60–71}$, $An_{39–54}$ and $An_{27–33}$ [where $An = Ca/(Ca + Na)$], with the more sodic compositions present in exsolution lamellae in clinopyroxene and in matrix plagioclase within well-equilibrated, symplectite-free samples. The orthoclase proportion is generally <3%.

Ilmenite is unzoned and occurs in minor quantities (<5 vol. %). The Fe/Ti ratio ranges from 0·906 to 1·004 and there is <0·05 Mg per formula unit $FeTiO_3$.

Amphibole is a major constituent (10–40 vol. %) of all analysed samples. It shows little intra-sample compositional variability, but significant differences between samples, with $Fe/(Fe + Mg)$ ranging from 0·42 to 0·72 (Table 2). Assuming all iron as Fe^{2+}, the amphibole grains range from pargasite to ferrohornblende and ferropargasite.

Biotite is present in most samples analysed (<10 vol. %). Biotite laths that are aligned parallel to S_2 contain between 2·0 and 5·6 wt % TiO_2 and up to 0·98 wt % F (Table 2). As with the other ferromagnesian minerals, biotite shows considerable inter-sample compositional variation, with $Fe/(Fe + Mg)$ ranging from 0·37 to 0·72. Randomly oriented biotite is compositionally indistinguishable from the syn-tectonic biotite.

Metapelitic gneiss

The peak (and earliest recognizable) metamorphic assemblage in the metapelitic rocks is Grt–Bt–Ky–Pl–Kfs–Qtz–Gr, corresponding to the upper amphibolite facies. Aligned elongate laths of kyanite, biotite and graphite define the S_2 fabric and are set in a matrix of strained quartz, plagioclase and K-feldspar. Garnet occurs as porphyroblasts, 2–5 mm in diameter, that are wrapped by the foliation. In high-strain zones the garnet occurs as σ-porphyroclasts that indicate a top-to-NW shear sense. Quartz, rutile, biotite, monazite, and zircon occur as inclusions in the garnet. The internal fabric is continuous with the external S_2, from which syn-tectonic (with respect to D_2) garnet growth is inferred. Kyanite grains vary in size from 0·5 mm to 5 mm, exhibit localized kinking and associated undulose extinction, and contain inclusions of biotite, quartz, monazite, zircon and rutile. No evidence of an earlier metamorphic event is preserved in the metapelite samples.

Retrograde metamorphic effects include sillimanite growth at the expense of kyanite, and muscovite growth at the expense of kyanite and/or sillimanite. In sillimanite- and muscovite-bearing domains, garnet is partially replaced by intergrowths of biotite and plagioclase. Rare local replacement of biotite by chlorite is limited to areas adjacent to syn-D_5 joints and fractures.

A total of 182 electron microprobe analyses were obtained of garnet, biotite and plagioclase (for representative analyses see Table 3). Garnet composition is dominated by almandine ($X_{Alm} = 72–79$, $X_{Pyr} = 12–20$, $X_{Gro} = 4–7$, $X_{Sps} = 2–4\%$). Its modal proportion is typically between 5 and 20 vol. %. In a particularly garnet-rich (45 vol. %) sample, a markedly higher grossular content (8–25%) was noted. Garnet grains in most samples are not zoned. The only exception is a systematic enrichment in X_{Gro} and corresponding depletion of X_{Alm} from core to rim in the garnet-rich sample, which might be a relic of prograde growth zonation reflecting progressive compression. Plagioclase constitutes between 5 and 15 vol. %. It is unzoned, has $An_{27–41}$ and X_{Or} of <0·015.

Modal proportions of biotite range from 5 to 30 vol. %, only exceeded in thin intercalations of biotite–garnet layers (40 vol. %). Aligned and randomly oriented biotite grains are compositionally similar ($X_{Fe} = 49–55\%$), both within and between samples (Table 3). Biotite in the biotite–garnet layers is more ferrous.

GEOTHERMOBAROMETRY
Metabasic rocks

The application of geothermobarometry to the metabasic rocks is complicated by their multi-stage metamorphic history. Quantifying $P–T$ for the early metamorphic stage is problematic, as the eclogite-facies assemblage was largely replaced by an amphibolite-facies assemblage, and the compositions of the original garnet and clinopyroxene most probably have changed.

Assuming that clinopyroxene containing albite-rich plagioclase exsolution lamellae represents the retrogressed equivalent of former omphacite (Boland & van Roermund, 1983) and that this replacement was isochemical, original omphacite compositions were approximated by reintegration of clinopyroxene and plagioclase volumes and compositions. Sample WBSV034 was found most suitable for this calculation, which follows that outlined by Markl & Bucher (1997). The modal abundances of plagioclase exsolution lamellae and host clinopyroxene were determined by point counting in texturally homogeneous parts of the section as respectively 43 and 57 vol. % clinopyroxene. The recalculated omphacite contains approximately 30% jadeite and 14–17% calcium tschermakite (Table 4). A minimum pressure of 12·9–14·3 kbar is estimated from these compositions by modelling the reaction

$$\text{jadeite} + \text{quartz} \rightarrow \text{albite} \qquad (3)$$
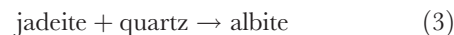
using THERMOCALC 2.75 (Powell et al., 1998).

Table 3: Representative electron microprobe analyses of garnet (Grt), plagioclase (Pl) and biotite (Bt) in metapelitic gneiss

Garnet and plagioclase

Sample:	WBSV025				WBSV084				WBSV110			
Locality:	72°35·630'S, 000°21·264'E				72°38·303'S, 000°26·655'E				72°39·211'S, 000°10·073'E			
Rock:	Grt–Ky gneiss				Grt–Ky gneiss				Grt–Bt layer			
Grain no.:	Grt-26 core	Grt-19 rim	Pl-2	Pl-5	Grt-12 core	Grt-15 rim	Pl-4	Pl-6	Grt-40 core	Grt-39 rim	Pl-3	Pl-7
SiO_2	36·63	36·36	62·64	62·43	37·06	35·88	60·26	60·88	37·25	37·42	59·27	59·37
TiO_2	0·00	0·00	0·00	0·00	0·00	0·00	0·00	0·00	0·00	0·00	0·00	0·00
Al_2O_3	21·22	21·14	24·87	25·89	21·94	22·73	25·66	25·72	21·09	21·11	26·96	26·08
Cr_2O_3	0·29	0·29	0·00	0·00	0·00	0·00	0·00	0·00	0·00	0·00	0·00	0·00
FeO	33·10	34·70	0·12	0·06	35·10	33·20	0·10	0·12	33·97	29·67	0·23	0·15
MnO	0·94	1·12	0·00	0·00	1·85	0·97	0·00	0·00	1·47	1·93	0·00	0·00
MgO	4·87	3·97	0·00	0·00	2·94	4·69	0·01	0·00	3·41	1·73	0·00	0·00
CaO	2·45	2·12	4·79	4·86	1·75	2·43	5·80	5·82	3·01	9·06	7·39	6·53
Na_2O	0·03	0·01	7·09	7·02	0·04	0·03	7·43	6·49	0·04	0·01	5·72	6·75
K_2O	0·00	0·00	0·12	0·14	0·00	0·00	0·00	0·00	0·00	0·00	0·11	0·17
F	n.d.	n.d.	n.d.	n.d.	n.d.	n.d.	n.d.	n.d.	n.d.	n.d.	n.d.	n.d.
Total	99·52	99·71	99·63	100·40	100·67	99·94	99·26	99·03	100·25	100·92	99·68	99·05
Si	2·94	2·94	2·76	2·73	2·96	2·87	2·69	2·71	2·98	2·98	2·64	2·66
Ti	0·00	0·00	0·00	0·00	0·00	0·00	0·00	0·00	0·00	0·00	0·00	0·00
Al	2·01	2·01	1·29	1·34	2·07	2·14	1·35	1·35	1·99	1·98	1·41	1·38
Cr	0·02	0·02	0·00	0·00	0·00	0·00	0·00	0·00	0·00	0·00	0·00	0·00
Fe	2·22	2·34	0·00	0·00	2·35	2·22	0·00	0·00	2·28	1·97	0·00	0·01
Mn	0·06	0·08	0·00	0·00	0·13	0·07	0·00	0·00	0·10	0·13	0·00	0·00
Mg	0·58	0·48	0·00	0·00	0·35	0·56	0·00	0·00	0·41	0·20	0·00	0·00
Ca	0·21	0·18	0·23	0·23	0·15	0·21	0·28	0·28	0·26	0·77	0·35	0·31
Na	0·00	0·00	0·61	0·60	0·01	0·00	0·64	0·56	0·01	0·00	0·49	0·59
K	0·00	0·00	0·01	0·01	0·00	0·00	0·00	0·00	0·00	0·00	0·01	0·01
Total	8·05	8·05	4·90	4·90	8·01	8·06	4·96	4·90	8·02	8·04	4·91	4·95

Biotite

Sample:	WBSV025		WBSV084		WBSV110	
Grain no.:	Bt-1 synfol.	Bt-12 synfol.	Bt-3 synfol.	Bt-6 rnd.	Bt-1 synfol.	Bt-7 rnd.
SiO_2	35·09	34·69	33·30	34·52	34·78	34·67
TiO_2	2·34	3·47	3·67	3·67	4·19	4·10
Al_2O_3	19·06	19·55	19·10	20·09	13·84	13·99
Cr_2O_3	0·00	0·00	0·00	0·00	0·00	0·00
FeO	18·76	19·65	18·40	18·85	26·76	26·42
MnO	0·00	0·03	0·04	0·03	0·10	0·10
MgO	9·86	9·07	9·63	9·22	7·90	7·25
CaO	0·20	0·00	0·00	0·00	0·18	0·18
Na_2O	0·19	0·19	0·12	0·11	0·13	0·00
K_2O	8·92	9·25	9·09	9·63	9·29	9·27
F	0·13	0·27	0·27	0·21	0·12	0·00
Total	94·56	96·17	93·62	96·33	97·29	95·99
Si	5·85	5·72	5·63	5·67	5·92	5·97
Al^{IV}	2·15	2·28	2·37	2·33	2·08	2·03
T-site	8·00	8·00	8·00	8·00	8·00	8·00
Al^{VI}	1·59	1·51	1·43	1·55	0·70	0·81
Ti	0·29	0·43	0·47	0·45	0·54	0·53
Cr	0·00	0·00	0·00	0·00	0·00	0·00
Fe	2·61	2·71	2·60	2·59	3·81	3·81
Mn	0·00	0·00	0·01	0·00	0·01	0·01
Mg	2·45	2·23	2·43	2·26	2·00	1·86
O-site	6·94	6·88	6·93	6·86	7·06	7·02
Ca	0·04	0	0·00	0·00	0·03	0·03
Na	0·06	0·06	0·04	0·03	0·04	0·00
K	1·90	1·95	1·96	2·02	2·02	2·04
A-site	1·99	2·01	2·00	2·05	2·10	2·07

Formulae based on 12 oxygens for garnet, eight for plagioclase, and 24(O + OH) for biotite; All iron reported as FeO; n.d., not determined; synfol., parallel to S_2; rnd., randomly oriented.

Table 4: Reintegrated omphacite compositions from four microdomains in sample WBSV034

	C2, P2	C3, P8	C10, P17	C4, P6
SiO_2	53·19	53·23	53·39	52·21
TiO_2	0·15	0·24	0·23	0·13
Al_2O_3	12·88	14·20	13·22	14·41
Cr_2O_3	0·02	0·01	0·02	0·02
FeO	4·89	5·58	5·29	5·66
MnO	0·04	0·06	0·05	0·05
MgO	7·70	7·40	7·37	6·90
CaO	16·46	15·85	15·98	15·43
Na_2O	3·90	3·88	4·04	4·03
K_2O	0·16	0·18	0·09	0·14
Total	99·39	100·63	99·68	98·98
X_{jd}	0·29	0·29	0·30	0·30
X_{CaTs}	0·14	0·17	0·14	0·17

C, clinopyroxene, P, plagioclase, C2, clinopyroxene analysis 2, etc.

Textural evidence of newly formed hornblende and plagioclase (of intermediate composition) being in equilibrium with the partially resorbed garnet in several of the metabasic rock samples opens up the possibility of placing constraints on the amphibolite-facies *P–T* conditions. Textural disequilibrium between biotite and the earlier-formed minerals precludes the use of geothermobarometry in the quantification of the retrograde *P–T* conditions.

The Grt–Hbl and Hbl–Pl geothermometers of Graham & Powell (1984) and Holland & Blundy (1994), and the Grt–Hbl–Pl–Qtz and Grt–Rt–Ilm–Pl–Qtz geobarometers of Kohn & Spear (1991) and Bohlen & Liotta (1986) were used. The edenite–tremolite geothermometer of Holland & Blundy (1994) was applied to all of the samples except WBSV066, for which the edenite–richterite geothermometer was preferred because of the absence of quartz. In each sample, *P–T* estimates were made for several microdomains in which the relevant phases appear to be in textural equilibrium. Samples WBSV034 and WBSV079 both contain clinopyroxene but only in the latter does this mineral appear to be in equilibrium with the amphibolite-facies assemblage. Consequently, the Grt–Cpx geothermometer (Ellis & Green, 1979; Krogh, 1988; Pattison & Newton, 1989; Ai, 1994) and Grt–Cpx–Pl–Qtz geobarometer (Newton & Perkins, 1982; Moecher *et al.*, 1988; Eckert *et al.*, 1991) were applied in an attempt to place further constraints on the *P–T* conditions. *P–T* estimates were obtained from several microdomains containing garnet and clinopyroxene, as well as such domains, in which garnet, plagioclase, clinopyroxene and quartz appear to be in textural equilibrium, using different combinations of the above

geothermobarometers. Results of the application of the various geothermobarometers are summarized in Tables 5 and 6.

In less equilibrated, symplectite-rich samples (WBSV034 and WBSV041), temperature estimates determined by the Grt–Hbl geothermometer are at variance with those obtained from the Hbl–Pl geothermometers. In these samples Fe–Mg exchange equilibrium between hornblende and garnet may not have been attained and, therefore, results from the Hbl–Pl thermometer are favoured.

The temperature and pressure ranges determined for the various samples using the Hbl–Pl geothermometer in combination with the Grt–Hbl–Pl–Qtz and Grt–Rt–Ilm–Pl–Qtz geobarometers are within error, both within and between samples. Pressure estimates obtained for the various samples using the Fe and Mg end-members of the Kohn & Spear (1991) geobarometers display some variation that is explainable by slight differences in garnet and amphibole mineral chemistry.

The combination of the Pattison & Newton (1989) thermometer, regardless of which barometer was used, when applied to the Grt–Cpx–Pl–Qtz microdomains in sample WBSV079, consistently returned temperatures of $\sim$100–110°C lower than the estimates in Table 5. Pressure estimates obtained using the Newton & Perkins (1982) and Eckert *et al.* (1991) geobarometers are generally lower (between $\sim$1·5 and 3·0 kbar) than those determined using the various Grt–Hbl–Pl–Qtz–Ilm–Rt geothermobarometers (Table 5), regardless of which thermometer was used. Consequently, results from the Ellis & Green (1979) and Moecher *et al.* (1988) thermobarometers are favoured. The similarity between the *P–T* estimates determined using these calibrations and the estimates presented in Table 5 suggests that local equilibrium may have been attained between garnet, clinopyroxene, plagioclase and quartz during M_{2b} in this sample. Combining the results of the various geothermobarometers results in an overall range in *P–T* estimates for M_{2b} of $T = 687$–758°C and $P = 9·4$–11·3 kbar.

The above results were compared with those obtained by applying the average *P–T* method (Powell & Holland, 1994) to garnet-bearing amphibolite samples using THERMOCALC version 2.75 (Powell *et al.*, 1998). Mineral analyses from microdomains in which all of the M_{2b} phases appear to be in textural equilibrium were selected for optimal geothermobarometry, and the activities of the various end-members were calculated using the program AX of T. Holland (available at http://www.esc.cam.ac.uk/astaff/holland/index.html). Average *P–T* values were calculated using the activities determined for the various end-members of garnet, ilmenite, hornblende, clinopyroxene and plagioclase, as well as quartz, rutile and titanite, where present, at estimated metamorphic temperatures. Average *P–T* calculations

Table 5: Results of the application of various geothermometers and geobarometers to amphibolite samples

Sample	Grt–Hbl	Hbl–Pl and Grt–Hbl–Pl–Qtz (Fe end-member)	Hbl–Pl and Grt–Hbl–Pl–Qtz (Mg end-member)	Hbl–Pl and Grt–Rt–Ilm–Pl–Qtz
WBSV031	663–738°C	703°C; 9·5 kbar	704°C; 9·6 kbar	707°C; 10·5 kbar
WBSV034	755–844°C	744°C; 9·7 kbar	745°C; 10·0 kbar	745°C; 10·5 kbar
WBSV041	914–1010°C	698°C; 8·6 kbar	699°C; 10·1 kbar	699°C; 9·8 kbar
WBSV066		*Hbl–Pl only*: 724°C at 9·2 kbar 729°C at 11·3 kbar		
WBSV079	689–704°C	739°C; 10·8 kbar	739°C; 10·4 kbar	739°C; 11·0 kbar

P–T estimates in columns 3, 4 and 5 are presented as *P–T* ranges at the intersection between results obtained from Hbl–Pl thermometry and Grt–Hbl–Pl–Qtz as well as Grt–Rt–Ilm–Pl–Qtz barometry (for calibrations used see text).

Table 6: Summary of geothermobarometric results for amphibolite

	NP	M	E
EG	726°C; 9·0 kbar	731°C; 11·0 kbar	727°C; 9·3 kbar
K	691°C; 8·7 kbar	697°C; 10·7 kbar	692°C; 9·0 kbar
PN	617°C; 8·1 kbar	628°C; 10·1 kbar	619°C; 8·4 kbar
A	638°C; 8·3 kbar	649°C; 10·3 kbar	640°C; 8·6 kbar

P–T estimates are presented as *P–T* ranges at the intersection between the respective thermometric and barometric results; NP, Newton & Perkins (1982); M, Moecher *et al.* (1988); E, Eckert *et al.* (1991); EG, Ellis & Green (1979); K, Krogh (1988); PN, Pattison & Newton (1989); A, Ai (1994).

Table 7: Average pressure and temperature estimates and fluid composition constraints for selected microdomains within pre-tectonic amphibolite from optimal geothermobarometry

Sample	Average *P–T* estimates*			Fluid composition*	
	T (°C)	*P* (kbar)	σ-fit	X_{CO_2}	X_{H_2O}
WBSV031	712 ± 70	9·6 ± 1·4	1·27	0·1	0·4
WBSV034†	742 ± 48	9·7 ± 1·0	1·13	0·1	0·2
	741 ± 54	10·2 ± 1·2	1·31	0·1	0·3
WBSV041	721 ± 64	9·0 ± 1·5	1·37	0·03	0·03
	710 ± 55	9·1 ± 1·4	1·38	0·03	0·03
WBSV079	749 ± 43	11·2 ± 0·9	1·09	0·1	0·3
	722 ± 37	10·6 ± 0·8	0·89	0·1	0·3
	735 ± 38	11·1 ± 0·8	1·00	0·1	0·3

*Obtained for σ-fit minima.
†Cpx not in equilibrium and thus excluded.

for all samples except WBSV041 yielded σ-fit values slightly larger than one, yet less than a maximum value required to pass a χ^2 test, indicating that the input data are broadly consistent with the final *P–T* estimate (Powell & Holland, 1994). The ferroactinolite end-member in sample WBSV041 was flagged as being a potential problem, because it has a high value of e^*_{fact}. Deletion of this end-member from the data file produced a set of results that passed the χ^2 test, and this revised *P–T* estimate was used.

Ignoring the effect of fluid pressure and composition resulted in average *P–T* estimates that are geologically unreasonable (in the range ∼800–1000°C and ∼11–13 kbar), with the associated errors being very large (up to ±100°C and ±3 kbar). Limited fluid activity is evident from the symplectitic textures (e.g. Messiga *et al.*, 1990). Powell & Holland (1994) suggested that the average fluid composition probably corresponds to that for which a minimum σ-fit is obtained in *P–T–X* calculations.

Consequently, average *P–T* estimates were modelled using different fluid compositions until a minimum value of σ-fit was obtained, resulting in $X_{CO_2} = 0·1$ and $X_{H_2O} = 0·2–0·4$ for samples WBSV031, WBSV034 and WBSV079, and $X_{CO_2} = X_{H_2O} = 0·03$ for WBSV041 (Table 7). Combining the results of the application of optimal geothermobarometry to the various samples results in an overall range in *P–T* estimates of *T* = 642–792°C and *P* = 7·7–11·9 kbar.

Metapelitic gneiss

The Grt–Bt thermometer (Holdaway, 2000) and Grt–Ky–Pl–Qtz barometer (Holdaway, 2001) were applied

Table 8: Pressure–temperature conditions at intersection between garnet–biotite thermometric and garnet–kyanite–plagioclase–quartz barometric results for different microdomains within three metapelitic gneiss samples

Sample	$P–T$ estimates
WBSV025	693°C; 8·1 kbar
	689°C; 7·9 kbar
	688°C; 7·8 kbar
WBSV084	686°C; 7·0 kbar
	690°C; 7·5 kbar
	683°C; 7·5 kbar
	677°C; 7·0 kbar
WBSV110*	702–707°C (r), 725–728°C (c)
	715–718°C (r), 738–741°C (c)
	650–653°C (r), 754–757°C (c)
	662–665°C (r), 763–767°C (c)

(r), rim; (c), core.
*Temperatures calculated for 7·0 and 8·0 kbar as no geobarometer is applicable to this sample.

to the selected metapelitic gneiss samples. Several microdomains in which garnet, biotite, kyanite (present only in samples WBSV025 and WBSV084), plagioclase and quartz appear to be in textural equilibrium were chosen for geothermobarometry. The employed geothermometer and geobarometer use the ferric iron estimates determined for natural reduced garnet [$Fe^{3+}/(Fe^{2+} + Fe^{3+}) = 0·03$] and biotite [$Fe^{3+}/(Fe^{2+} + Fe^{3+}) = 0·116$] from Maine (Guidotti & Dyar, 1991; Holdaway *et al.*, 1997) and these estimates were also used in this study to maintain internal consistency. Thermobarometric calculations were made with the programs GB, GASP and GBGASP of Holdaway (2000, 2001), using $T = 680°C$ and $P = 7$ kbar as input $P–T$ values for samples WBSV025 and WBSV084, and $T = 720°C$ and $P = 7$ kbar for sample WBSV110. The $P–T$ data and ranges were calculated in a similar way to those obtained for the metabasic rocks. The results of the application of these geothermobarometers to the three samples of metapelitic gneiss are presented in Table 8. Estimates of amphibolite-facies $P–T$ conditions in samples WBSV025 and WBSV084 are $T = 677–693°C$; $P = 7·0–8·1$ kbar, whereas T estimates for sample WBSV110, using various garnet rim and core compositions and assuming $P = 7·0$ and $8·0$ kbar, range between 650–718°C and 725–767°C, respectively.

No meaningful $P–T$ estimates could be obtained for a wide range of input conditions using the average $P–T$ method. The lack of constraints on the fluid–melt phase hampers the application of the average $P–T$ method to the metapelitic rocks, which have clearly been affected by fluid infiltration and partial melting.

$P–T$ path

Three stages of metamorphic recrystallization are distinguished in the studied rocks. The first stage is evident only in garnet–clinopyroxene relics within strain-protected boudins that record a $P > 12·9$ kbar. No reliable temperature estimate could be derived from these relics, but from the widespread decompression textures preserved in many amphibolite samples, similar temperatures to those of the subsequent amphibolite-facies stage are inferred. Most of the mineral assemblages formed during the second stage, and $P–T$ conditions calculated for individual metabasic rock samples, using various geothermobarometers, are all within the corresponding errors obtained from the application of the average $P–T$ method (Table 7). The overall ranges in $P–T$ estimates for the metabasic rocks are consistent with field observations and independent petrogenetic constraints. They plot between the water-saturated granite solidus and the vapour-absent muscovite melting reaction in the NKASH system, which controls the solidus relationships in the NCKFMASH system (White *et al.*, 2001). This is in agreement with the field evidence of partial melting in the metapelitic rocks. The $P–T$ estimates plot on the low-temperature side of the basalt solidus as determined for intermediate water activities ($a_{H_2O} = 0·6$; Holloway & Burnham, 1972). Low fluid activities derived for the pre-tectonic metabasic rocks are therefore consistent with a lack of partial melting in these rocks. Overall, a temperature between 687 and 758°C and a pressure between 9·4 and 11·3 kbar are considered the best estimates for this second metamorphic stage.

The, on average, slightly lower temperatures and pressures calculated for the metapelitic samples (Table 8) relative to the metabasic rocks indicate that the less competent metapelitic rocks have been subject to more extensive re-equilibration on the retrograde path. This is supported by the limited development of sillimanite at the expense of kyanite. As the garnet–biotite thermometer and the garnet–aluminium silicate–quartz–plagioclase barometer probably behave differently during the retrograde history as a result of the differences in relative efficiencies of component exchange between phases (e.g. Fe–Mg exchange is relatively faster and more efficient than Ca, Si and Al exchange), the $P–T$ estimates (7·0–7·5 kbar, *c.* 690°C) may not represent a true point on the $P–T$ path, but rather a combination based on P and T attained at different times. This retrograde overprint, representing the third metamorphic stage, affected the rocks after the fabric-forming deformation, as evident from the abundant post-tectonic growth of biotite in highly variable proportions in most rock types, including the rims of amphibolite boudins.

GEOCHRONOLOGY
U–Pb SHRIMP dating of zircon and monazite

Mineral separation was carried out on selected samples using standard heavy liquid and magnetic separation techniques. Individual zircon and monazite grains, and *in situ* monazite grains were analysed using the SHRIMP I and II ion microprobes at the Research School of Earth Sciences, Australian National University (ANU), Canberra. Cathodoluminescence (CL) imaging of zircon grains and backscatter electron (BSE) imaging of monazite grains was conducted prior to isotope analysis. SHRIMP analytical techniques have been described by Compston *et al.* (1984), Ireland & Gibson (1998) and Williams (1998). Isotopic ratios and inter-element fractionation were monitored by continuous reference to zircon (SL13) and monazite (from Thompson Mine, Canada) standards, fragments of which were mounted with each sample. The $^{206}Pb/^{238}U$ ratio in the unknown zircon grains was normalized to 0·0928 for SL13 (equivalent to an age of 572 Ma). $^{206}Pb/^{238}U$ ratios were normalized to 0·3152 for the monazite standard (1766 Ma). For all samples the SHRIMP analyses (Electronic Appendix 2) consisted of six scans through the mass range. Where $^{207}Pb/^{206}Pb$ ages are quoted or calculated, common Pb corrections were made using the measured $^{204}Pb/^{206}Pb$ composition and the relevant model Pb composition from Cumming & Richards (1975). For analyses with very low Th/U ratios (generally ≤0·01), correction for common Pb using measured ^{208}Pb was preferred. U–Pb ages were calculated from the $^{206}Pb/^{238}U$ compositions, with the correction for common Pb being made using the measured $^{207}Pb/^{206}Pb$ and $^{206}Pb/^{238}U$ as described by Compston *et al.* (1984). All ages quoted in this study were calculated using the recommended decay constants of Steiger & Jäger (1977). Statistical analysis of the data was conducted using the program ISOPLOT/EX (Ludwig, 2000).

The isotope data were supplemented by *in situ* analyses of the REE concentrations in selected zircon and monazite grains, using electron microprobe and laser ablation inductively coupled mass spectrometry (LA-ICP-MS) techniques at the Department of Geological Sciences, University of Cape Town. For the latter, a Perkin Elmer Elan 6000 instrument, coupled to a Cetac LSX-200 LA module with a 266 nm frequency-quadrupled Nd–YAG laser was employed. The NIST 610 and 612 glass standards were used for zircon analyses, whereas an in-house standard of homogeneous monazite was used for the calibration of the monazite analyses. Lower limits of detection are typically below 20 ppb for the REE, and typical precision and accuracy range from 1 to 10 relative %.

Oldest pre-tectonic granitic gneiss (WBSV065)

The oldest pre-tectonic granitic gneiss forms the northernmost outcrop of the Skarsnuten group of nunataks (Fig. 3). It is overlain by the quartzofeldspathic rocks of the Fuglefjellet Formation and has been intruded by numerous pre-tectonic mafic bodies. Leucosome development is extremely limited and the granitic gneiss exhibits a weaker foliation than the overlying quartzofeldspathic gneiss.

All zircon grains display well-developed compositional growth zonation under CL imaging (Fig. 6), which is probably a primary magmatic structure (Vavra, 1990). Zircon overgrowths are generally absent, but irregularly shaped areas, characterized by bright CL, that are discordant to the growth zonation are present in a few of the grains. Results and their interpretation are given in Table 9 and Fig. 7. The general absence of overgrowths, in combination with the observation that this body is less intensely foliated than rocks of the overlying paragneiss sequence, suggests that it may have been an effective strain resistor during tectono-metamorphic events subsequent to its formation at 1132 ± 16 Ma.

Metapelitic gneiss (WBSV025)

The metapelitic gneiss of the Rootshorga Formation is part of a paragneiss package that overlies the granitic gneiss of the Jutulrøra Formation and that is cut by the pre-tectonic tabular gneissic granite of the Sveabreen Suite. Dark brown cores that are surrounded by relatively clear zircon overgrowths are visible in a few of the zircon grains in transmitted light. CL imaging revealed that the majority of the grains are homogeneous and do not display a complex internal structure (Fig. 6h). The cores that are visible under transmitted light in a few of the grains are generally indistinguishable from the rims on the CL images, although a few grains contain small irregularly shaped areas of brighter CL that are interpreted as highly resorbed cores. These features suggest that the unstructured zircon was probably formed as a result of almost complete dissolution of older zircon grains during a subsequent (metamorphic) event. The fact that non-metamict zircon remains closed to Pb diffusion at most crustal temperatures (Mezger & Krogstad, 1997; Cherniak & Watson, 2000), together with the observation that the irregularly shaped older cores, where present, are locally crosscut by younger zircon, argues against the formation of the unstructured zircon as a result of diffusional resetting of older grains. Results are given in Table 9 and Fig. 7h.

Two grains containing older cores (grains 21 and 43) were analysed (both cores and rims) for REE by LA-ICP-MS (Fig. 8). The cores and the rims of both grains are enriched in heavy REE (HREE) and display negative Eu
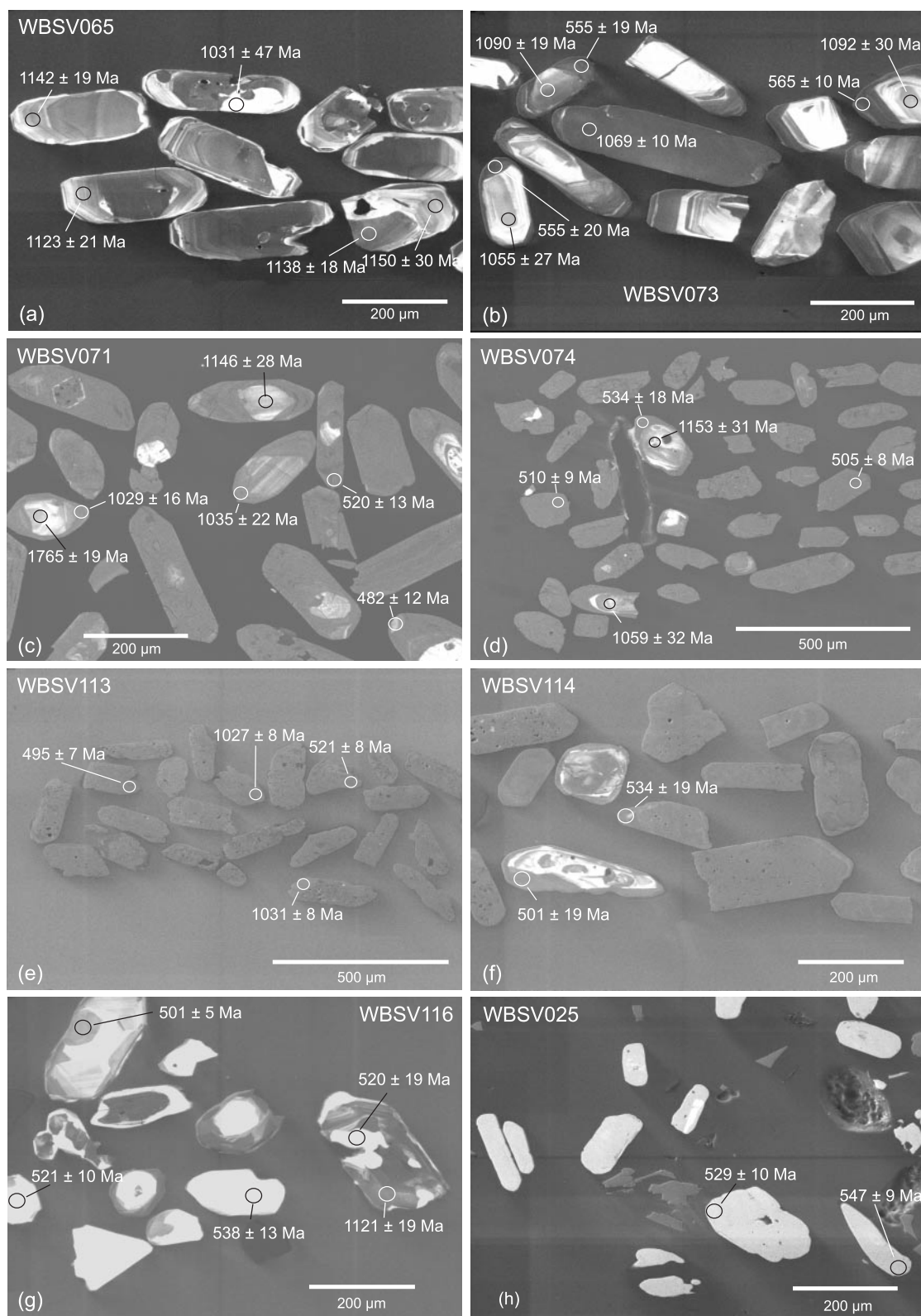
Fig. 6. CL images of zircon grains from (a) oldest, pre-tectonic granite gneiss, (b) tabular pre-tectonic granite gneiss, (c–g) various syn-tectonic leucosome domains, and (h) metapelitic paragneiss; the ages around 500 Ma for samples WBSV071 and WBSV116 are $^{206}Pb/^{238}U$ ages; all other dates are $^{207}Pb/^{206}Pb$ ages.

Table 9: Summary of SHRIMP U–Pb single zircon spot analyses

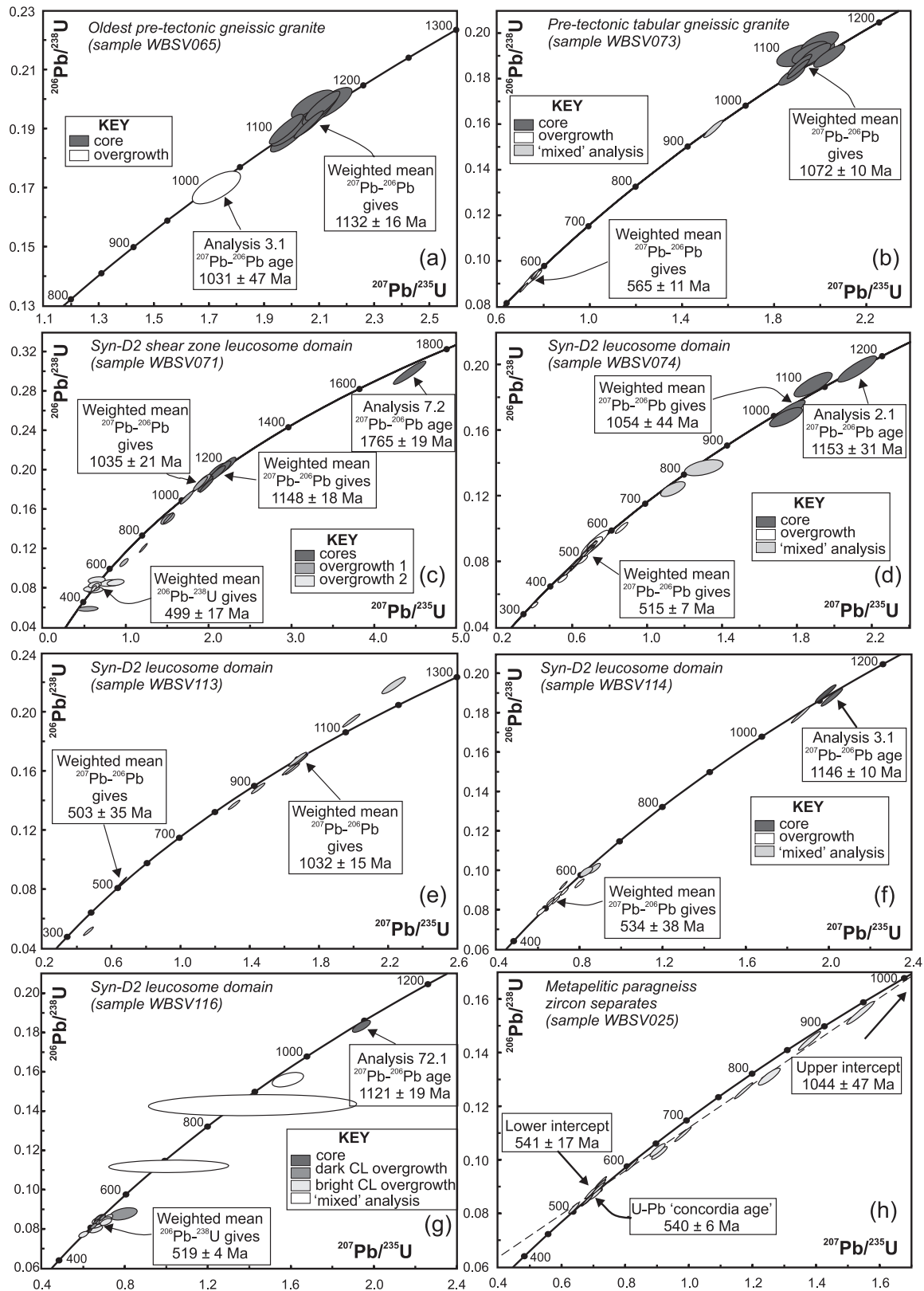| Sample, rock type, co-ordinates	Zircon size (μm), appearance, crystal forms	Interpreted age, type of age (Ma)	Number of analyses, MSWD, probability of fit, discordance	Th/U
WBSV065 Pre-tectonic granitic gneiss 72°30·432'S, 000°22·891'E	130–350, colourless, zoned, {100}{101}	Intrusion (core), ^{207}Pb–^{206}Pb: 1132 ± 16 Metamorphism (rim), ^{207}Pb–^{206}Pb: 1031 ± 47	10, 1·5, 0·16, <7% 1	0·28 0·15
WBSV025 Metapelitic gneiss 72°35·630'S, 000°21·264'E	<70–350, yellow–brown, rounded, {100}{101}	Metamorphism I Concordia—upper intercept: 1044 ± 47 Metamorphism II Concordia—lower intercept: 540 ± 6 ^{206}Pb–^{238}U: 541 ± 8 ^{207}Pb–^{206}Pb: 540 ± 9	22, 3·1 9, 0·012, 0·91, <9% 9, 2·1, 0·017, <9% 9, 2·1, 0·018; <9%	<0·02 <0·02
WBSV073 Tabular pre-tectonic gneissic granite 72°34·824'S, 000°32·591'E	170–440, pale yellow, ovoid, zoned, {100}{101}	Intrusion (core), ^{207}Pb–^{206}Pb: 1072 ± 10 Metamorphism I (overgrowth), ^{207}Pb–^{206}Pb: 996 ± 17 Metamorphism II (rim), ^{207}Pb–^{206}Pb: 565 ± 11, ^{206}Pb–^{238}U: 563 ± 14	9, 0·27, 0·98, <8% 1 spot, 5% 6, 1·01, 0·41, <3% 6, 2·5, 0·031, <3%	0·18–0·58 <0·01 <0·01
WBSV071 Syn-tectonic leucosome 72°35·270'S, 000°32·000'E	90–410, colourless–brown, complex zonation, {100}{101}	Inherited core, ^{207}Pb–^{206}Pb: 1765 ± 19 Inherited magmatic core, ^{207}Pb–^{206}Pb: 1148 ± 18 Metamorphism I (rim), ^{207}Pb–^{206}Pb: 1035 ± 21, Concordia—upper intercept: 1050 +31/–27 Metamorphism II, lower intercept, ^{206}Pb–^{238}U: 499 ± 17	1 spot 7, 0·60, 0·73, <6% 5, 0·68, 0·61, <5% 8, 1·9, variable 6, 1·7, 0·13, 3–10%	0·33 0·07 0·03
WBSV074 Syn-tectonic leucosome 72°34·795'S, 000°24·236'E	100–800, colourless–brown, metamict, {100}{101}	Inherited magmatic core, ^{207}Pb–^{206}Pb: 1153 ± 31, ^{207}Pb–^{206}Pb: 1054 ± 44 Metamorphism I (rim), ^{207}Pb–^{206}Pb: 515 ± 7, ^{206}Pb–^{238}U: 520 ± 16	1 spot, 2% 3, 0·61, 0·54, variable 14, 1·14, 0·32, <10% 14, 0·30, 0·00, <10%	0·27 0·01
WBSV113 S_2-parallel leucosome 72°31·243'S, 000°22·955'E	100–300, dark brown, metamict, {100}{101}	Metamorphism I, ^{207}Pb–^{206}Pb: 1032 ± 15 Metamorphism II, ^{207}Pb–^{206}Pb: 503 ± 35, ^{206}Pb–^{238}U: 511 ± 36	5, 2·1, 0·079, <7% 3, 3·3, 0·036, <5% 3, 3·6, 0·027, <5%	0·02–0·05 <0·05
WBSV114 S_2-parallel leucosome 72°31·243'S, 000°22·955'E	100–500, brown, metamict, {100}{101}	Inherited magmatic core, ^{207}Pb–^{206}Pb: 1146 ± 10, 1090 ± 11 Metamorphism (rim), ^{207}Pb–^{206}Pb: 525 ± 35, ^{206}Pb–^{238}U: 524 ± 24	1 spot, 3% 2, 0·57, 0·45, <2% 7, 6·8, 0·00, <6% 7, 11·0, 0·00, <6%	0·57–0·62 0·04 <0·05
WBSV116 Leucosome in syn-D_2 *en echelon* tension gashes 72°31·243'S, 000°22·955'E	100–350, colourless, complex zonation, {100}{101}	Inherited magmatic core ^{207}Pb–^{206}Pb: 1121 ± 19 Metamorphism (overgrowth), ^{206}Pb–^{238}U: 519 ± 8	1 spot, 3% 14, 1·05, 0·39, <10%	0·34 <0·02

Fig. 7. U–Pb concordia plots showing SHRIMP analyses for zircon grains from (a) oldest, pre-tectonic granite gneiss, (b) tabular pre-tectonic granite gneiss, (c–g) various syn-tectonic leucosome domains, and (h) metapelitic paragneiss (see Fig. 6).
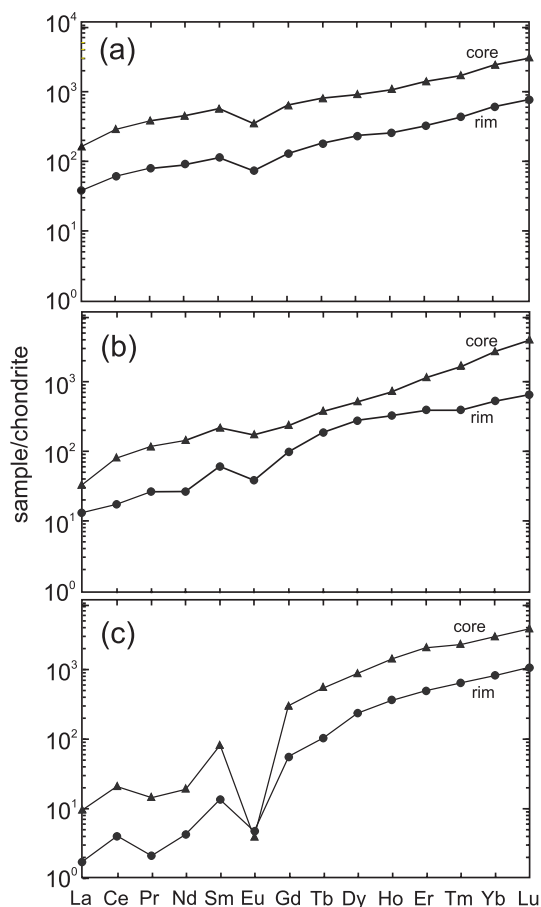
Fig. 8. Chondrite-normalized rare earth element patterns for core and rim of zircon grains 21 (a) and 43 (b) of metapelitic gneiss sample WBSV025 and grain 33 from sample WBSV073 (c); normalization values from Sun & McDonough (1989).

Formation (Groenewald *et al.*, 1995; Board, 2002). The tabular orthogneiss is intensely migmatized and homogeneous gneissic granite without significant leucosome development was sampled from the Rootshorga massif.

The prismatic zircon grains in this rock display rounded terminations, in places leading to an ovoid morphology. Oscillatory growth zonation is developed within all of the zircon grains (Fig. 6b). Dark unzoned zircon overgrowths are commonly developed along the outer margins of the grains and at grain terminations, and are discordant to the growth zonation. Results are given in Table 9 and Fig. 7b.

Chondrite-normalized REE patterns obtained for the magmatic core (^{207}Pb–^{206}Pb age = 1055 ± 27 Ma; 1σ) and overgrowth (^{207}Pb–^{206}Pb age = 555 ± 20 Ma; 1σ) of grain 33 (Fig. 8c) display a HREE enrichment (Yb$_N$/La$_N$ = 308 and 544, respectively) and strong negative Eu anomalies, but differ in terms of the degree of REE enrichment relative to chondrite. The core is more enriched in REE than the overgrowth. The magmatic cores and secondary overgrowths are consequently interpreted as two generations of zircon on the basis of the textural, chemical and geochronological features presented.

The low Th/U ratios of the secondary overgrowths (Table 9) and their lower REE content suggest that they crystallized during high-grade metamorphism (Williams & Claesson, 1987; Hoskin & Black, 2000). The age of the oldest zircon population (1072 ± 10 Ma) is considered to represent the age of crystallization of the pre-tectonic tabular granite, whereas the 565 ± 11 Ma age is interpreted as dating a metamorphic event. The *c.* 996 Ma age is possibly of no geological significance and is due to the probe spot on a very thin rim having overlapped with the older core.

Syn-tectonic leucosome domains

Syn-tectonic leucosomes are developed within all pre-tectonic rocks of the southern H.U. Sverdrupfjella. Although two generations were recognized at Skarsnuten, only one generation was found in the Rootshorga and Hamrane groups of nunataks. Four samples of the older generation of leucosome (WBSV071, WBSV074, WBSV113 and WBSV114) and one sample of the younger generation (WBSV116) were analysed by SHRIMP II (Electronic Appendix 2).

Sample WBSV071
Zircon in this semipelitic paragneiss-hosted syn-tectonic leucosome within a ductile shear zone with a top-to-NW shear sense from northern Rootshorga has a complex structure as revealed by CL images, with three types being recognized (Fig. 6c). Older cores displaying magmatic oscillatory compositional zoning are preserved.

anomalies. The cores of both grains are more enriched in REE than the rims. Both the REE distribution and geochronology are consistent with the interpretation of two zircon generations. Almost complete dissolution of older grains (defined by the eight older discordant analyses) with variable degrees of Pb loss during a subsequent event is inferred. The morphology and chemistry of the majority of the zircon grains indicate that the *c.* 540 Ma age dates a metamorphic event. The upper intercept age (*c.* 1044 Ma) is difficult to interpret because of the imprecision in the estimate. It is, however, within error of ages obtained on a number of other samples (see below), which are interpreted as reflecting an earlier metamorphic event.

Tabular pre-tectonic gneissic granite (WBSV073)
The tabular pre-tectonic gneissic granite bodies are intrusive into the paragneiss sequence of the Rootshorga

These are overgrown by weakly cathodoluminescent rims that are discordant to the growth zonation in the cores. A second type of zircon overgrowth is indicated by the presence of unzoned zircon embayments that are characterized by a slightly brighter CL than the first overgrowth type. These embayments are generally developed along the outer margins of the grain and at grain terminations and cut across the first overgrowth type.

The results obtained from 24 analyses of 21 zircon grains are plotted on a U–Pb concordia diagram (Fig. 7c) and summarized in Table 9. The textural, chemical and geochronological characteristics of the zircon grains in this sample indicate three zircon generations. By analogy with sample WBSV073, the low Th/U ratio (<0.1) of the two overgrowth types is interpreted as indicative of a metamorphic origin. The fact that the syn-tectonic leucosome cuts both generations of pre-tectonic felsic intrusives indicates that they must be younger than $c.$ 1072 Ma. Consequently, the older cores are interpreted as resorbed portions of zircon grains inherited from the host paragneiss. The two generations of zircon overgrowth indicate disturbance of the U–Pb isotopic system during two periods of metamorphism, at $c.$ 1035 Ma and $c.$ 499 Ma. The discordant nature of the younger metamorphic overgrowth suggests Pb loss and therefore the $c.$ 499 Ma age is, at best, a minimum age for this generation. As zircon with metamorphic chemical characteristics can be precipitated from metamorphic fluids and partial melts (Williams *et al.*, 1996; Roberts & Finger, 1997), the leucosome domain may either be a Grenvillian body that was reworked during Pan-African metamorphism or a Pan-African domain that contains inherited zircon grains in which relics of an older metamorphic event are recorded.

Sample WBSV074

Zircon grains from this foliation-parallel leucosome within a tabular pre-tectonic orthogneiss from northwestern Rootshorga produce dark, featureless CL images, although compositionally zoned cores characterized by a brighter CL are present in a few cases (Fig. 6d). Unstructured zircon cuts across the growth zonation displayed by the cores and contains isolated remnants of this zonation in some grains.

The results of 28 analyses on 19 zircon grains are presented on a U–Pb concordia diagram (Fig. 7d) and in Table 9. The textural, geochronological and chemical characteristics indicate two generations of zircon growth, and the low Th/U ratio of the overgrowths is consistent with a metamorphic origin. The $c.$ 1153 Ma age is similar to that of the magmatic zircon grains of the oldest granitic intrusive (WBSV065) and the inherited zircon cores of sample WBSV071. The $c.$ 1054 Ma age for the compositionally zoned zircon cores of this sample is within error

of the age of the magmatic zircon from the tabular orthogneiss (sample WBSV073) that hosts the leucosome domain from which this sample was collected. Consequently, the older magmatic zircon cores are interpreted as portions of grains inherited from the host gneiss. As the majority of the zircon crystals in this sample consist entirely of unstructured zircon with metamorphic chemical characteristics, except for the few grains in which older cores are preserved, and as no meaningful ages between $c.$ 1054 Ma and $c.$ 515 Ma were determined, the latter is interpreted as dating zircon growth during crystallization of the leucosome.

Sample WBSV113

Leucosome that is parallel to S_2 and up to 60 cm wide contains zircon grains that display a homogeneous dark CL image (Fig. 6e). Because of their highly metamict nature, analyses were limited to clear undamaged parts of individual grains.

The results of 13 analyses on 11 grains are presented in Fig. 7e and Table 9. The older population is statistically indistinguishable from the oldest zircon overgrowth of sample WBSV071, and is interpreted as recording a metamorphic event at $c.$ 1032 Ma. The younger population is considered a product from a subsequent metamorphic event at $c.$ 503 Ma that induced partial Pb loss in some of the older zircon grains. The leucosome domain may therefore either be a syntectonic body of Grenvillian age that was reworked during a Pan-African tectono-thermal episode or a wholly Pan-African body that contains relics of an earlier metamorphic event.

Sample WBSV114

This sample comes from the same outcrop as the previous one, but represents a very thin leucosome vein parallel to S_2. Most of the zircon grains in this sample are characterized by a very dark CL and zoning is not obvious or is obscured by radiogenic damage (Fig. 6f). In some grains relics of older cores were identified by their bright CL. Some of the cores display a weak oscillatory zonation that is truncated by the darker overgrowths, whereas others exhibit a patchy zonation, suggesting that they have been extensively recrystallized.

The results of 13 analyses on 10 relatively clear zircon grains are plotted on Fig. 7f and summarized in Table 9. A ^{207}Pb–^{206}Pb age of $c.$ 1146 Ma obtained on cores is within error of that determined for the oldest granitic body (WBSV065) and therefore these cores are interpreted as inherited grains. A relatively concordant age of close to 1090 Ma obtained on cores is difficult to interpret. It might date a geological event, but it might also represent a 'mixed' age, because of a very low Th/U ratio and patchy zonation under CL. The ^{207}Pb–^{206}Pb
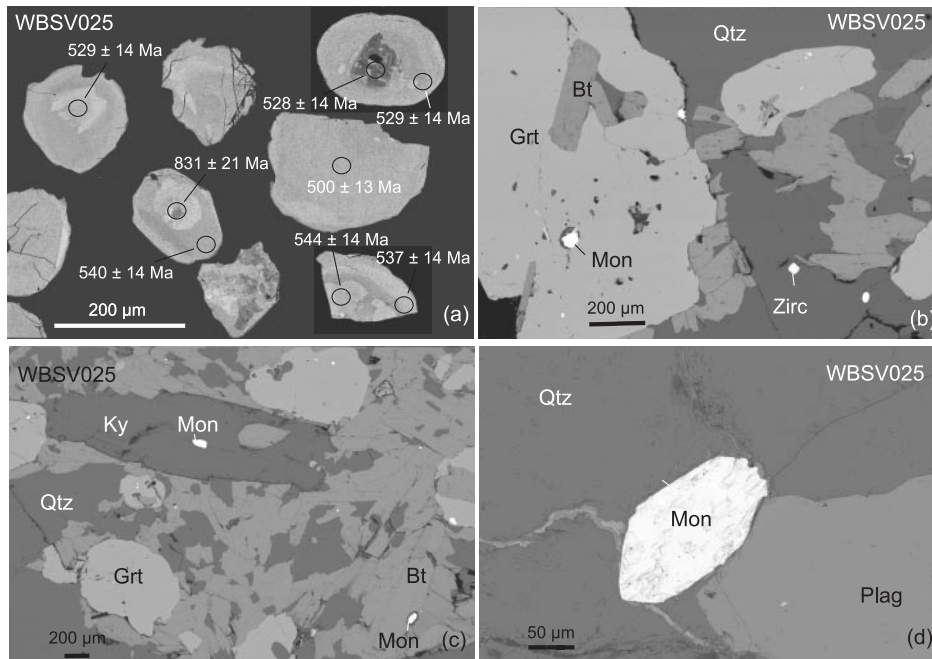
Fig. 9. BSE images of monazite separates (a) and *in situ* monazite grains (b–d) from paragneiss sample WBSV025. The dates shown in (a) are $^{206}Pb/^{238}U$ ages. Monazite (Mon) occurs as inclusions in garnet (Grt), kyanite (Ky) and biotite (Bt), and in the matrix between quartz (Qtz) and plagioclase (Plag).

age of *c.* 534 Ma obtained on overgrowths is interpreted as dating zircon growth during crystallization of the leucosome.

Sample WBSV116

This sample comes from the same outcrop as the previous two, but represents a younger leucosome generation that occurs in *en echelon* tension gashes defining syn-D_2 top-to-NW shearing. The zircon grains display a complex internal structure under CL with three types being recognized: older cores are present in some grains and two types of zircon overgrowth can be distinguished (Fig. 6g). The older cores display oscillatory compositional zonation indicating that they crystallized out of a melt. The one type of zircon overgrowth is characterized by bright CL and occurs as rims to the older zircon cores, as discrete structureless grains and as cores to those grains that are rimmed by the second overgrowth type. Overgrowths of this first type truncate the compositional banding of the older cores. The second type of zircon overgrowth is characterized by dark CL and occurs as rims and as embayments that are locally discordant to the bright CL overgrowths. In some grains zircon with bright CL forms a rim to structureless zircon cores characterized by a dark CL, suggesting that the two types of zircon overgrowth may be coeval.

Results obtained on 22 analyses from 18 grains are plotted on a U–Pb concordia diagram (Fig. 7g) and summarized in Table 9. Whereas the textural evidence

indicates three types of zircon, the chemical and isotope data are consistent with the zircon overgrowths having formed penecontemporaneously during the crystallization of the leucosome. Consequently, the leucosome is considered to be of Pan-African age.

U–Pb SHRIMP dating of monazite

Monazite occurs in pelitic paragneiss as clear, yellow, angular to rounded, anhedral grains, ranging in size from 130 to 390 μm. Although BSE imaging revealed that the majority of the monazite grains are homogeneous, small dark irregularly shaped cores are present in a few grains as well as diffuse areas with a brighter signal (Fig. 9a). SHRIMP I was used to obtain 20 analyses from 14 grains (Fig. 10a). Three analyses of small dark cores (8.1, 15.1, 20.1) yielded $^{207}Pb–^{206}Pb$ ages (1σ errors) of 1014 ± 8 Ma (10% discordant), 1077 ± 8 Ma (4% discordant) and 953 ± 6 Ma (12% discordant), respectively. The remaining analyses were obtained from both the brighter 'cores' as well as the homogeneous rims of the monazite grains and can be combined to obtain a weighted mean ^{207}Pb-corrected $^{206}Pb/^{238}U$ age of 524 ± 8 Ma (MSWD = 1·19; probability of fit = 0·27). This is statistically similar to a U–Pb 'concordia age' (calculated using the $^{206}Pb/^{238}U$ and $^{207}Pb/^{235}U$ ratios, errors and error correlation; Ludwig, 1998) of 528 ± 6 Ma (MSWD = 1·7; probability of fit = 0·19) determined for 14 of the 17 analyses (rejecting those more

Fig. 11. Chondrite-normalized rare earth element patterns for monazite separates from paragneiss sample WBSV025; normalization values from Sun & McDonough (1989).
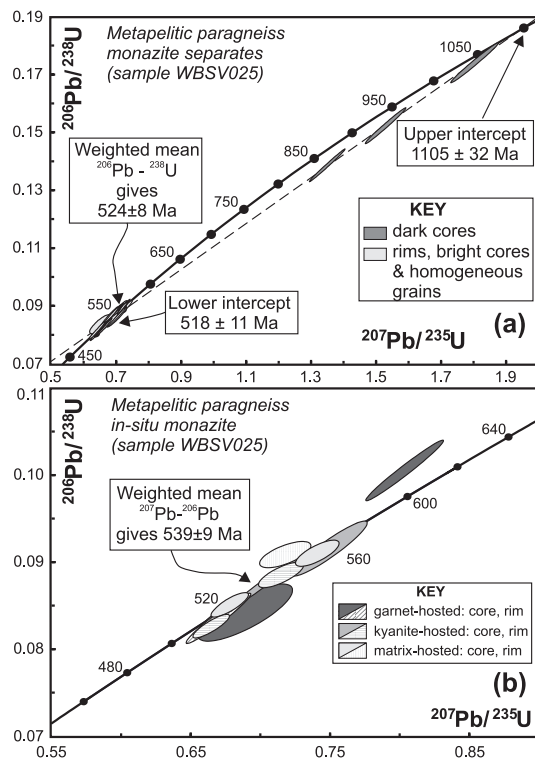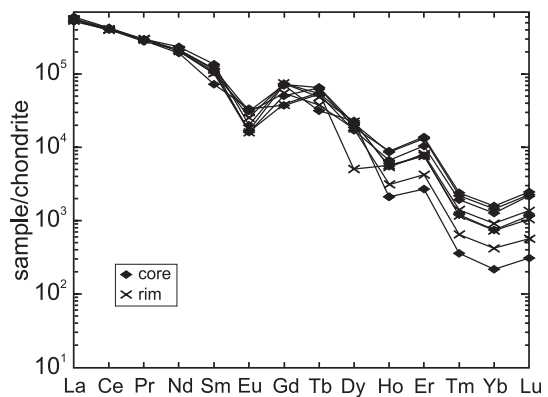
Fig. 10. U–Pb concordia plots showing SHRIMP analyses for monazite separates (a) and *in situ* monazite grains (b) from paragneiss sample WBSV025.

than 6% discordant). The three older cores plot on a discordia with the *c.* 524 Ma population; regression of all of the data yields an upper intercept age of 1105 ± 32 Ma and a lower intercept age of 518 ± 11 Ma (MSWD = 0·93; probability of fit = 0·54).

Chondrite-normalized REE patterns were obtained for eight grains (five cores and three rims; Fig. 11). Both core and rim analyses exhibit very similar light REE-enriched patterns (mean core and rim La_N/Yb_N = 868 and 877, respectively) that display identical negative Eu anomalies (mean Eu/Eu* = 0·32). The older cores are interpreted as highly resorbed portions of inherited grains that may have been formed at *c.* 1105 Ma. This age is within error of both the oldest granitic body and the tabular gneissic granite. It is, therefore, unclear as to whether the older cores represent portions of detrital monazite grains or whether they are remnants of monazite grains that were formed in response to the intrusion of the tabular granitic bodies (the sample was collected ~120 m stratigraphically below one of these intrusions) at *c.* 1072 Ma. The older cores underwent partial Pb loss during the *c.* 524 Ma event, as evidenced by the fact that their data plot on a discordia with those of the younger monazite generation.

In the absence of a systematic relationship between older cores and grain size—the older cores are present

in smaller grains (~180–200 μm) whereas most of the grains, irrespective of size, have cores and rims of Pan-African age—we argue against resetting of the monazite grains by diffusion. Experimental work on monazite (Seydoux-Guillame *et al.*, 2001) suggests that resetting of this mineral is controlled by dissolution–precipitation rather than diffusion. Consequently, the younger monazite generation is considered to have formed by precipitation following dissolution of the older inherited monazite and therefore the age determined for the majority of the monazite grains is interpreted as a crystallization age dating a metamorphic event at *c.* 524 Ma.

To test this interpretation, monazite inclusions in syn-tectonic, S_2-defining minerals, such as kyanite, biotite and garnet (Fig. 9b–d), were analysed *in situ*. BSE imaging did not reveal any internal structure in the monazite grains. Ten analyses were performed on six grains (two garnet-hosted, two kyanite-hosted and two matrix-hosted), including core and rim analyses on four of the grains, using SHRIMP II. Ignoring outlier values (analyses 2.1 and 3.2 for ^{207}Pb–^{206}Pb data and analyses 5.2 and 7.1 for ^{206}Pb–^{238}U data), the data can be combined to obtain similar weighted mean ^{207}Pb–^{206}Pb and ^{206}Pb–^{238}U ages: 539 ± 9 Ma (MSWD = 0·79; probability of fit = 0·59) and 544 ± 16 Ma (MSWD = 5·5; probability of fit = 0·04), respectively. These ages are within error of the age determined for the monazite separates and are similar to an upper intercept age of 548 ± 19 Ma (MSWD = 1·5; probability of fit = 0·14), obtained by regression of all of the data points. There is no systematic variation in monazite age as a function of spot location within a given grain (i.e. core or rim) or as a function of grain position in the sample. It has been demonstrated (Montel *et al.*, 2000) that minerals such as garnet can effectively shield included monazite grains from resetting at temperatures well above their closure temperature to Pb diffusion ($725 \pm 25°C$). As the texturally homogeneous monazite grains in this sample do not display variable ages as a

function of host mineral, and as analyses were also made on monazite inclusions in garnet, the age determined for the *in situ* monazite grains is interpreted as a crystallization age that provides the so far best age constraint on the S_2 fabric.

Conventional U–Pb dating of zircon

Zircon from an example of widespread post-tectonic monzogranitic dykes was dated by conventional dissolution techniques as no post-crystallization disturbance of the U–Th–Pb isotope system at elevated temperatures was expected. Clear, light brown, non-metamict inclusion-free zircon grains, between 2 and 15 μg in mass, were recovered from sample WBSV069 collected from a post-tectonic monzogranitic dyke that cross-cuts the oldest pre-tectonic granitic gneiss at Skarsnuten (72°30·432′S, 000°22·891′E). All of the grains selected for analysis were euhedral, of dipyramidal prismatic habit with dominance of the {100} prism and {101} pyramidal forms. Nine zircon grains were analysed at the Department of Geological Sciences, University of Cape Town, following the techniques described by Frimmel *et al.* (2001) and using a VG Sector mass spectrometer. The laboratory Pb blank was better than 5 pg and this amount was subtracted from all analyses.

Although no optical difference could be seen between the grains, two populations can be distinguished on the basis of their $^{207}Pb/^{235}U$ and $^{206}Pb/^{238}U$ ratios (Fig. 12). Regression of all of the data of the older population (higher $^{207}Pb/^{235}U$ and $^{206}Pb/^{238}U$ ratios; $n = 6$) gave an upper intercept age of 1086 ± 31 Ma (MSWD = 44). Rejecting the analysis with the largest error (grain 7) results in a slightly more precise age of 1095 ± 23 Ma (MSWD = 43; Fig. 12a). The data display variable degrees of discordance indicating Pb loss subsequent to the formation of these grains. The large error attached to the lower intercept age (219 ± 230 Ma) prevents a meaningful interpretation. Regression of the data from two of the three younger grains (rejecting the data from grain 3 because of the large error in the analysis) yielded an upper intercept age of 480 ± 10 Ma (Fig. 12b). The lower intercept age of these discordant data (−1 ± 20 Ma) is consistent with present-day Pb loss. The age of the older population is within error of the age of the oldest granitic body (1132 ± 16 Ma) and therefore the older zircon grains are interpreted as being inherited from the host rock. The upper intercept age of the younger population (480 ± 10 Ma) is interpreted as approximating the crystallization age of the intrusive body.

$^{40}Ar–^{39}Ar$ dating of hornblende and biotite

Fabric-forming (syn-S_2) hornblende and biotite grains were separated from three samples of garnet amphibolite,
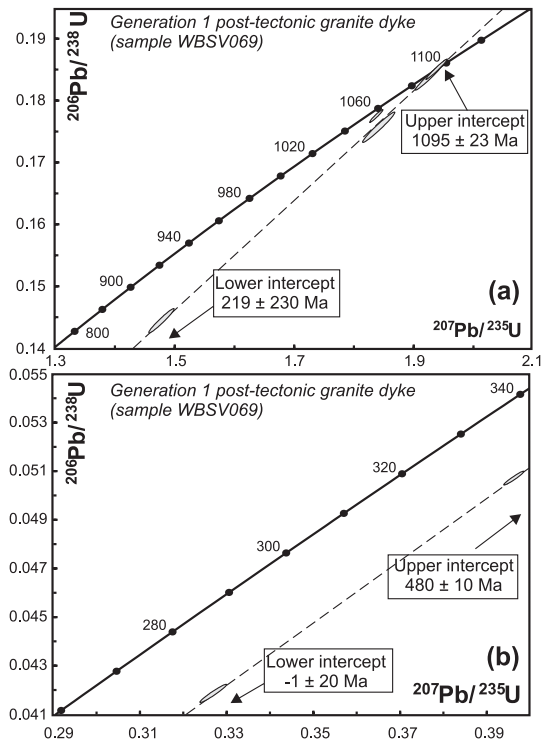

Fig. 12. U–Pb concordia diagram for a post-tectonic monzogranitic dyke (WBSV069): (a) inherited zircon grains, (b) highly discordant syn-intrusive zircon grains.

two samples of amphibolite and one garnet–hornblende–biotite paragneiss from across the H.U. Sverdrupfjella. The $^{40}Ar–^{39}Ar$ method was used to date these mineral separates at the Institute of Geology, University of Vienna, following the techniques described by Frimmel & Frank (1998). As the peak metamorphic temperature exceeded the closure temperature to argon diffusion in hornblende (∼500°C, Harrison & Fitzgerald, 1986) and biotite (∼320°C, Von Blanckenburg *et al.*, 1989), the Ar–Ar age data provide insights into the post-peak cooling history. Details of these are given in Electronic Appendix 3.

The $^{40}Ar–^{39}Ar$ hornblende-cooling ages for all analysed samples are very similar and within mutual error, clustering around 486 ± 5 Ma except for the two oldest ages obtained (496 ± 4 and 499 ± 4 Ma), which might be due to the presence of some excess ^{40}Ar. Either the rocks cooled below 500°C (post-M_{2c}) around 486 Ma, implying a relatively slow cooling rate of 4 deg/Myr, or they experienced reheating above 500°C subsequent to Pan-African deformation and metamorphism around 540 Ma. The presence of hornblende relics that yielded higher $^{40}Ar–^{39}Ar$ ages of *c.* 520 Ma in sample KK12 points to incomplete resetting of an older amphibole, formed during the M_{2b} event, during a subsequent reheating event. The age of such a reheating event
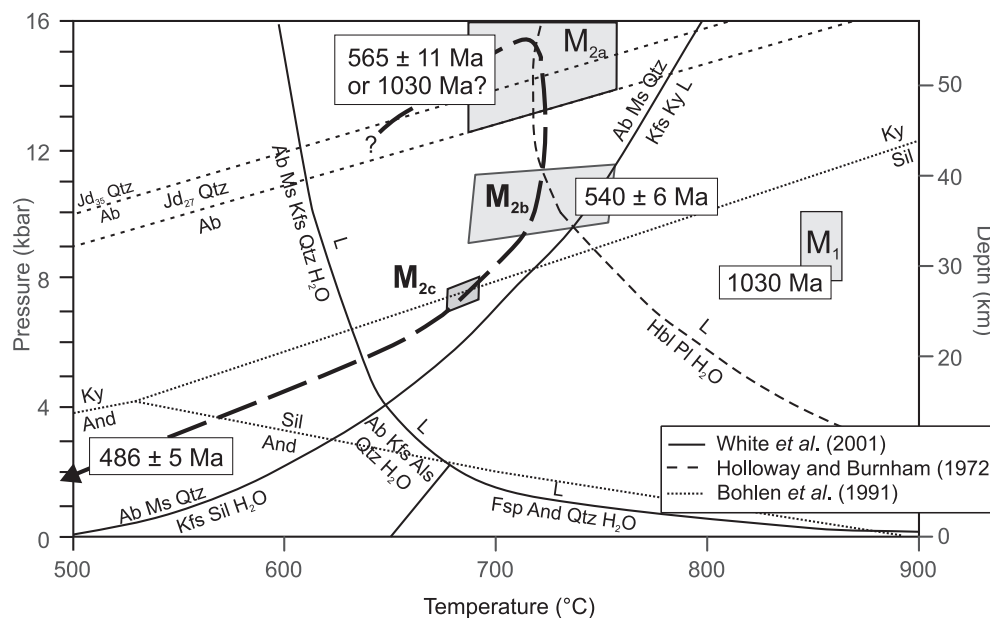
Fig. 13. Suggested Pan-African pressure–temperature–time path for amphibolite and metapelitic gneiss from the H.U. Sverdrupfjella; M_1 from Groenewald & Hunter (1991), M_{2a} pressure constrained from calculated omphacite compositions in garnet–clinopyroxene relics, M_{2b} P–T conditions from equilibrated amphibolite, M_{2c} conditions from metapelites; Al_2SiO_5 equilibria, granitic and basaltic solidus curves shown for reference; depth scale based on an average crustal density of $2 \cdot 8\,g/cm^3$.

coincides with the emplacement of the abundant post-tectonic $480 \pm 10\,Ma$ monzogranitic dykes. The ^{40}Ar–^{39}Ar biotite age spectra indicate incorporation of variable amounts of excess ^{40}Ar in most samples. Identical age data obtained for both biotite and hornblende ($488 \pm 4\,Ma$) in sample JE39 may indicate rapid cooling subsequent to the emplacement of the post-tectonic felsic dykes.

DISCUSSION AND CONCLUSIONS

Our new geochronological data on zircon overgrowths indicate two distinct phases of high-grade metamorphism, one between 1040 and $1030\,Ma$ (M_1), and another between c. 565 and c. $499\,Ma$ (M_2). The $539\,Ma$ age obtained for monazite inclusions in penetrative fabric-defining minerals provides the most reliable constraint not only on the timing of regional metamorphism but also on that of dominant top-to-NW shearing in the southern H.U. Sverdrupfjella. In contrast to previous models (Grantham *et al.*, 1995), this deformation is Pan-African in age, which is further supported by secondary zircon overgrowths within syn-kinematic leucosome. The fact that the U–Pb 'concordia age' ($540 \pm 6\,Ma$), weighted mean ^{207}Pb–^{206}Pb age ($540 \pm 9\,Ma$), weighted mean ^{206}Pb–^{238}U age ($541 \pm 8\,Ma$) and lower intercept age ($541 \pm 17\,Ma$) of the metamorphic zircon, the weighted mean ^{207}Pb–^{206}Pb ($539 \pm 9\,Ma$), weighted mean ^{206}Pb–^{238}U ($544 \pm 16\,Ma$) and upper intercept ($548 \pm 19\,Ma$) ages of the *in situ* monazite, the U–Pb 'concordia age'

($528 \pm 6\,Ma$) of the monazite separates in sample WBSV025, and the relatively imprecise zircon overgrowth ages in samples WBSV113 ($503 \pm 35\,Ma$) and WBSV114 ($534 \pm 38\,Ma$) are statistically indistinguishable indicates a major, penetrative Pan-African tectono-thermal overprint at c. $540\,Ma$. All the younger ages determined for zircon overgrowths in other samples (Table 9) are minimum ages because of the discordant nature of the analyses.

The earliest metamorphic stage recorded in the study area reflects eclogite-facies conditions. Although this metamorphic stage remains to be dated reliably and could correspond to late Mesoproterozoic metamorphism (M_1), an early Pan-African age (M_{2a}) is favoured (Fig. 13), for three reasons: (1) the preservation of widespread symplectitic decompression textures is inconsistent with prolonged heating and/or hydration as might be expected if eclogite- and amphibolite-facies metamorphism were caused by two entirely different metamorphic cycles; (2) so far only granulite-facies metamorphism, reflecting a very different geothermal gradient, has been documented for M_1; (3) limited evidence of an earlier Pan-African metamorphic stage exists in the form of a zircon overgrowth age of $565 \pm 16\,Ma$. This evidence is only circumstantial, but if the eclogite-facies metamorphism led directly to regional syn-kinematic amphibolite-facies (M_{2b}) and retrograde, post-tectonic metamorphism (M_{2c}), it would define a coherent clockwise P–T–t path that is consistent with a scenario of considerable crustal thickening in

Pan-African times as is indicated now for the northern Maud Belt. Burial of supracrustal rocks to depths of at least 47–52 km would have been followed by exhumation to ∼34–41 km at *c.* 540 Ma. Retrograde amphibolite-facies metamorphism outlasted the penetrative deformation and eventually involved widespread K-metasomatism (M_{2c}). The latter has not been dated directly but, based on the Ar–Ar data, must be either older than or overlaps in time with post-tectonic intrusion of *c.* 480 Ma monzogranitic plutons, stocks and dykes throughout the northern parts of the belt.

The suggested model of an extensive tectono-thermal rather than purely thermal Pan-African overprint is in good agreement with evidence presented from adjacent areas to the south. Neoproterozoic oceanic crust has been reported from the Shackleton Range (Talarico *et al.*, 1999). Closer to the study area, from the southwestern part of the Maud Belt, mafic dykes of E-type MORB geochemistry with an age of 586 ± 7 Ma have been reported (Bauer *et al.*, 2003*a*). Although no juvenile Pan-African crust has been documented from the Maud Belt, the eclogite-facies relics described in this study could be an indication of early Pan-African subduction and associated accretion and/or continental collision, thus implying the existence of an intervening Neoproterozoic ocean of unknown width. Such a model of amalgamation of various Mesoproterozoic metamorphic blocks during Pan-African orogeny is also supported by palaeomagnetic data (Gose *et al.*, 1997). Whether the resulting suture represents the principal boundary between East and West Gondwana (Grunow *et al.*, 1996; Shackleton, 1996) remains, however, an unresolved question [see, for comparison, Jacobs & Thomas (2002)].

Considerable Pan-African crustal thickening suggested for the northern Maud Belt, and by analogy with a similar structural trend also for the central Maud Belt, implies that previous palaeogeographical reconstructions of the Maud Belt for the late Mesoproterozic must be viewed with caution. Any older, i.e. Grenvillian-age, structures and mineral assemblages would have been largely obliterated. Consequently, kinematic models that assume top-to-NW thrusting during a major Grenvillian tectono-thermal event (Groenewald *et al.*, 1995; Bauer *et al.*, 2003*b*) become problematic. In spite of the extensive Pan-African overprint, at least a partial reconstruction of a complex Mesoproterozoic tectonothermal history is possible (Fig. 14). It starts with the formation of a volcanic arc, the age of which is constrained by the oldest granitic body in the southern H.U. Sverdrupfjella (1132 ± 16 Ma) and inherited magmatic zircon cores (1146 ± 10 Ma, 1121 ± 19 Ma), in perfect agreement with previous constraints on the age of that arc elsewhere (Jacobs *et al.*, 2003; Frimmel, 2004). This date also provides an upper age limit for the overlying paragneiss sequence and the various generations of mafic and felsic intrusive rocks. The paragneiss sequence must have been deposited before *c.* 1072 Ma, the age of the intrusive tabular granitic gneiss. No radiometric data exist for the pre-tectonic mafic bodies but an age younger than that of the tabular granitic gneiss is inferred from field relationships. From the age spectrum for inherited zircon cores, derivation of the paragneiss protolith from the erosion of the 1132 Ma gneissic granite is indicated, with a minor component also from a Palaeoproterozoic (*c.* 1765 Ma) source.

The older metamorphic zircon overgrowths (*c.* 1044 and *c.* 1031 Ma) testify to late Mesoproterozoic high-grade metamorphism (M_1), in agreement with results obtained previously for the southwestern part of the belt in Heimefrontfjella (Arndt *et al.*, 1991; Jacobs *et al.*, 2003) and the Kirwanveggen (Harris, 1999; Jackson, 1999). Evidence of this event is missing in the northeasternmost part of the belt (Paulsson & Austrheim, 2003), where a more intense Pan-African reworking of the crust might have led to a complete obliteration of earlier metamorphic features. The *P–T* conditions for M_1 remain enigmatic, and, apart from the presence of pre-tectonic (with respect of Pan-African deformation) leucosome, a granulite-facies mineral assemblage reported from a shielded, anhydrous core in a mafic boudin in the northeastern H.U. Sverdrupfjella provides so far the best *P–T* estimates for M_1 (Fig. 13, Groenewald *et al.*, 1995).

Comparison of our results with those available from the southwestern portion of the Maud Belt (Jacobs *et al.*, 2003) and the continuation of the belt towards the NE into central Dronning Maud Land (Jacobs *et al.*, 1998) shows that the northern Maud Belt takes an intermediate position with regard to the extent of Pan-African reworking of Mesoproterozoic crust. In the SW, the discrete Heimfront Shear Zone separates a granulite-facies metamorphic terrane with little Pan-African overprint in the west, from polymetamorphic terranes that have experienced amphibolite-facies Pan-African overprint in the east. In central Dronning Maud Land, Pan-African metamorphism reaching upper granulite-facies conditions and voluminous Pan-African melt production obliterated almost all earlier features. This study documents that the northern Maud Belt has experienced Pan-African deformation at upper amphibolite-facies conditions, presumably resulting from decompression after eclogite-facies conditions, not only along discrete shear zones but also across the width of the belt. Considering the top-to-NW transport direction, it is speculated that the Pan-African orogenic front is located between the northern Maud Belt and the Grunehogna Province to the west, from where it continues into the Heimefront Shear Zone further SW (Fig. 2). Thus our results confirm the contention that the Maud Belt is the continuation of the East African orogenic belt into East Antarctica.
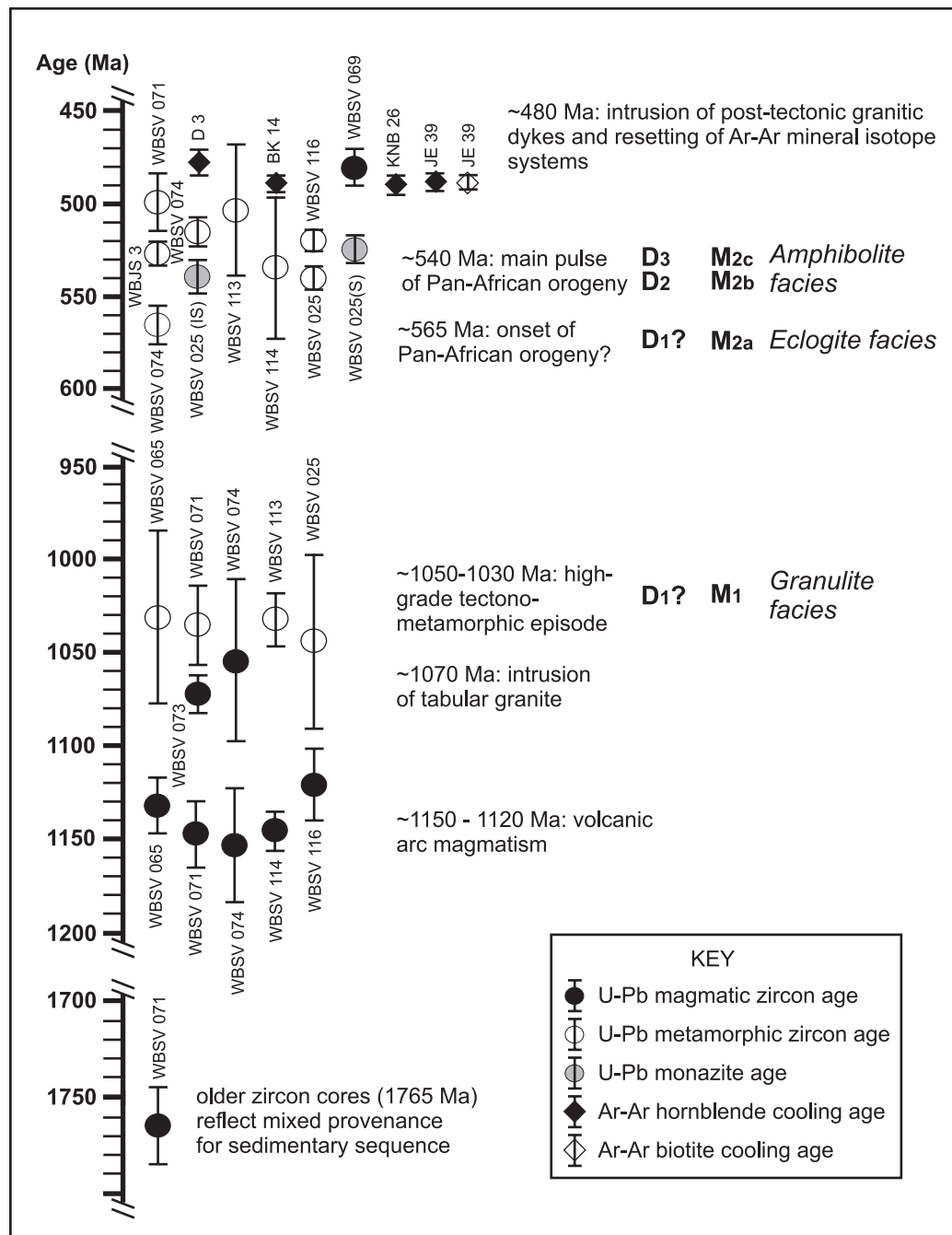
Fig. 14. Synoptic interpretation of the tectono-thermal evolution of the northern Maud Belt in H.U. Sverdrupfjella, based on most reliable radiometric age data; error bars correspond to age uncertainties for individual samples.

SUPPLEMENTARY DATA

Supplementary data for this paper are available at *Journal of Petrology* online.

REFERENCES

Ai, Y. (1994). A revision of the garnet–clinopyroxene Fe^{2+}–Mg exchange geothermometer. *Contributions to Mineralogy and Petrology* **115**, 467–473.

Arndt, N. T., Todt, W., Chauvel, C., Tapfer, M. & Weber, K. (1991). U–Pb zircon age and Nd isotopic composition of granitoids, charnockites and supracrustal rocks from Heimefrontfjella, Antarctica. *Geologische Rundschau* **80**, 759–777.

Bauer, W., Fielitz, W., Jacobs, J., Fanning, C. M. & Spaeth, G. (2003a). Mafic dykes from Heimefrontfjella and implications for the post-Grenvillian to pre-Pan-African geological evolution of western Dronning Maud Land, Antarctica. *Antarctic Science* **15**, 379–391.

Bauer, W., Jacobs, J., Fanning, C. M. & Schmidt, R. (2003b). Late Mesoproterozoic arc and back-arc volcanism in the Heimefrontfjella (East Antarctica) and implications for the palaeogeography at the southeastern margin of the Kaapvaal–Grunehogna Craton. *Gondwana Research* **6**, 449–465.

Board, W. S. (2002). Tectonothermal evolution of the southern H.U. Sverdrupfjella, western Dronning Maud Land, Antarctica. Ph.D. thesis, University of Cape Town, 205 pp.

Boger, S. D., Wilson, C. J. L. & Fanning, C. M. (2001). Early Palaeozoic tectonism within the East Antarctic craton: the final suture between east and west Gondwana? *Geology* **29**, 463–466.

Bohlen, S. R. & Liotta, J. J. (1986). A barometer for garnet amphibolites and garnet granulites. *Journal of Petrology* **27**, 1025–1034.

Bohlen, S. R., Montana, A. & Kerrick, D. M. (1991). Precise determinations of the equilibria kyanite = sillimanite and kyanite = andalusite and a revised triple point for Al_2SiO_5 polymorphs. *American Mineralogist* **76**, 677–680.

Boland, J. N. & van Roermund, H. L. M. (1983). Mechanisms of exsolution in omphacites from high temperature, type B eclogites. *Physics and Chemistry of Minerals* **9**, 30–37.

Cherniak, D. J. & Watson, E. B. (2000). Pb diffusion in zircon. *Chemical Geology* **172**, 5–24.

Compston, W., Williams, I. S. & Meyer, C. (1984). U–Pb geochronology of zircons from lunar breccia 73217 using a sensitive high mass-resolution ion microprobe. *Journal of Geophysical Research, Supplement* **89**, B525–B534.

Cumming, G. L. & Richards, J. R. (1975). Ore lead isotope ratios in a continuously changing Earth. *Earth and Planetary Science Letters* **28**, 155–171.

Dirks, P. H. G. M., Carson, C. J. & Wilson, C. J. L. (1993). The deformation history of the Larsemann Hills, Prydz Bay; the importance of the Pan-African (500 Ma) in East Antarctica. *Antarctic Science* **5**, 179–193.

Eckert, J. O. J., Newton, R. C. & Kleppa, O. J. (1991). The ?H of reaction and recalibration of garnet–pyroxene–plagioclase–quartz geobarometers in the CMAS system by solution calorimetry. *American Mineralogist* **76**, 148–160.

Ellis, D. J. & Green, D. H. (1979). An experimental study of the effect of Ca upon garnet–clinopyroxene Fe–Mg exchange equilibria. *Contributions to Mineralogy and Petrology* **71**, 13–22.

Fitzsimons, I. C. W. (2000a). Grenville-age basement provinces in East Antarctica: evidence for three separate collisional orogens. *Geology* **28**, 879–882.

Fitzsimons, I. C. W. (2000b). A review of tectonic events in the East Antarctic Shield and their implications for Gondwana and earlier supercontinents. *Journal of African Earth Sciences* **31**, 3–23.

Fitzsimons, I. C. W., Kinny, P. D. & Harley, S. L. (1997). Two stages of zircon and monazite growth in anatectic leucogneiss: SHRIMP constraints on the duration and intensity of Pan-African metamorphism in Prydz Bay, East Antarctica. *Terra Nova* **9**, 47–51.

Frimmel, H. E. (2004). Formation of a late Mesoproterozoic supercontinent: the South Africa–East Antarctica connection. In: Eriksson, P. G., Altermann, W., Nelson, D. R., Mueller, W. U. & Catuneanu, O. (eds) *The Precambrian Earth: Tempos and Events. Developments in Precambrian Geology* **12**, 240–255.

Frimmel, H. E. & Frank, W. (1998). Neoproterozoic tectono-thermal evolution of the Gariep Belt and its basement, Namibia/South Africa. *Precambrian Research* **90**, 1–28.

Frimmel, H. E., Zartman, R. E. & Späth, A. (2001). Dating Neoproterozoic continental break-up in the Richtersveld Igneous Complex, South Africa. *Journal of Geology* **109**, 493–508.

Golynsky, A. & Jacobs, J. (2001). Grenville-age versus Pan-African magnetic anomaly imprints in Western Dronning Maud Land, East Antarctica. *Journal of Geology* **109**, 136–142.

Gose, W. A., Helper, M. A., Connelly, J. N., Hutson, F. E. & Dalziel, I. W. D. (1997). Paleomagnetic data and U–Pb isotopic age determinations from Coats Land, Antarctica: implications for Neoproterozoic plate reconstructions. *Journal of Geophysical Research* **102**, 7887–7902.

Graham, C. M. & Powell, R. (1984). A garnet–hornblende geothermometer: calibration, testing, and application to the Pelona Schist, Southern California. *Journal of Metamorphic Geology* **2**, 13–31.

Grantham, G. H., Groenewald, P. B. & Hunter, D. R. (1988). Geology of the northern H.U. Sverdrupfjella, western Dronning Maud Land, and implications for Gondwana reconstructions. *South African Journal of Antarctic Research* **18**, 2–10.

Grantham, G. H., Jackson, C., Moyes, A. B., Groenewald, P. B., Harris, P. D., Ferrar, G. & Krynauw, J. R. (1995). The tectonothermal evolution of the Kirwanveggen–H.U. Sverdrupfjella areas, Dronning Maud Land, Antarctica. *Precambrian Research* **75**, 209–229.

Groenewald, P. B. & Hunter, D. R. (1991). Granulites of the northern H.U. Sverdrupfjella, western Dronning Maud Land: metamorphic history from garnet–pyroxene assemblages, coronas and hydration reactions. In: Thomson, M. R. A., Crame, J. A. & Thomson, J. W. (eds) *Geological Evolution of Antarctica*. Cambridge: Cambridge University Press, pp. 61–66.

Groenewald, P. B., Moyes, A. B., Grantham, G. H. & Krynauw, J. R. (1995). East Antarctic crustal evolution: geological constraints and modelling in western Dronning Maud Land. *Precambrian Research* **75**, 231–250.

Grosch, E. & Frimmel, H. E. (2004). Metamorphic evidence for a major Pan-African thrust between the Archaean Grunehogna Craton and the Mesoproterozoic Maud Belt, western Dronning Maud Land, East Antarctica. *Extended Abstracts, Geoscience Africa 2004, 12–16 July 2004*. Johannesburg: University of the Witwatersrand, pp. 227–228.

Grunow, A., Henson, R. & Wilson, T. (1996). Were aspects of Pan-African deformation linked to Iapetus opening? *Geology* **24**, 1063–1066.

Guidotti, C. V. & Dyar, M. D. (1991). Ferric iron in metamorphic biotite and its petrological and crystallochemical implications. *American Mineralogist* **76**, 161–175.

Harris, C. & Grantham, G. H. (1993). Geology and petrogenesis of the Straumsvola nepheline syenite complex, Dronning Maud Land, Antarctica. *Geological Magazine* **130**, 513–532.

Harris, P. D. (1999). The geological evolution of Neumayerskarvet in the Northern Kirwanveggen, Western Dronning Maud Land, Antarctica. Ph.D. thesis, Rand Afrikaans University, Johannesburg, 249 pp.

Harris, P. D., Moyes, A. B., Fanning, C. M. & Armstrong, R. A. (1995). Zircon ion microprobe results from the Maudheim high-grade gneiss terrane, western Dronning Maud Land, Antarctica. In: Barton, J. M. J. & Copperthwaite, Y. E. (eds) *Centennial Geocongress (1995)*. Johannesburg: Geological Society of South Africa, pp. 240–243.

Harrison, T. M. & Fitzgerald, J. D. (1986). Exsolution in hornblende and its consequences for $^{40}Ar/^{39}Ar$ age spectra and closure temperature. *Geochimica et Cosmochimica Acta* **50**, 247–253.

Hoffman, P. F. (1991). Did the breakout of Laurentia turn Gondwanaland inside-out? *Science* **252**, 1409–1412.

Holdaway, M. J. (2000). Application of new experimental and garnet Margules data to the garnet–biotite geothermometer. *American Mineralogist* **85**, 881–892.

Holdaway, M. J. (2001). Recalibration of the GASP geobarometer in light of recent garnet and plagioclase activity models and versions of the garnet–biotite geothermometer. *American Mineralogist* **86**, 1117–1129.

Holdaway, M. J., Mukhopadhyay, B., Dyar, M. D., Guidotti, C. V. & Dultrow, B. L. (1997). Garnet–biotite geothermometry revised: new Margules parameters and a natural specimen data set from Maine. *American Mineralogist* **82**, 582–595.

Holland, T. & Blundy, J. (1994). Non-ideal interactions in calcic amphiboles and their bearing on amphibole–plagioclase thermometry. *Contributions to Mineralogy and Petrology* **116**, 433–447.

Holloway, J. R. & Burnham, C. W. (1972). Melting relations of basalt with equilibrium water pressure less than total pressure. *Journal of Petrology* **13**, 1–29.

Hoskin, P. W. O. & Black, L. P. (2000). Metamorphic zircon formation by solid-state recrystallisation of protolith igneous zircon. *Journal of Metamorphic Geology* **18**, 423–439.

Ireland, T. R. & Gibson, G. M. (1998). SHRIMP monazite and zircon geochronology of high-grade metamorphism in New Zealand. *Journal of Metamorphic Geology* **16**, 149–167.

Jackson, C. (1999). *Characterization of Mesoproterozoic to Palaeozoic Crustal Evolution of Western Dronning Maud Land. Study 3: Deformational History and Thermochronology of the Central Kirwanveggen*. Pretoria: Department of Environmental Affairs and Tourism, 80 pp.

Jacobs, J. & Thomas, R. J. (2002). The Mozambique Belt from an East Antarctic perspective. In: Gamble, J. A., Skinner, D. N. B. & Henry, S. (eds) *Antarctica at the Close of a Millennium. Royal Society of New Zealand Bulletin* **35**, 3–18.

Jacobs, J., Fanning, C. M., Henjes-Kunst, F., Olesch, M. & Paech, H.-S. (1998). Continuation of the Mozambique Belt into East Antarctica: Grenville-age metamorphism and polyphase Pan-African high-grade events in central Dronning Maud Land. *Journal of Geology* **106**, 385–406.

Jacobs, J., Hansen, B. T., Henjes-Kunst, F., Thomas, R. J., Bauer, W., Weber, K., Armstrong, R. A. & Cornell, D. H. (1999). New age constraints on the Proterozoic/lower Palaeozoic evolution of Heimefrontfjella, East Antarctica, and its bearing on Rodinia/Gondwana correlations. *Terra Antartica* **6**, 377–389.

Jacobs, J., Fanning, C. M. & Bauer, W. (2003). Timing of Grenville-age vs. Pan-African medium- to high grade metamorphism in western Dronning Maud Land (East Antarctica). *Precambrian Research* **125**, 1–20.

Kohn, M. J. & Spear, F. S. (1991). Error propagation for barometers: 2. Application to rocks. *American Mineralogist* **76**, 138–147.

Kretz, R. (1983). Symbols for rock-forming minerals. *American Mineralogist* **68**, 277–279.

Krogh, E. J. (1988). The garnet–clinopyroxene Fe–Mg geothermometer—a reinterpretation of existing experimental data. *Contributions to Mineralogy and Petrology* **99**, 44–48.

Krynauw, J. R. (1996). A review of the geology of East Antarctica, with special reference to the *c.* 1000 Ma and *c.* 500 Ma events. *Terra Antartica* **3**, 77–89.

Leake, B. E., Woolley, A. R., Arps, C. E. S., *et al.* (1997). Nomenclature of Amphiboles: Report of the Subcommittee on Amphiboles of the International Mineralogical Association Commission on New Minerals and Mineral Names. *Mineralogical Magazine* **61**, 295–321.

Ludwig, K. R. (1998). On the treatment of concordant uranium–lead ages. *Geochimica et Cosmochimica Acta* **62**, 665–676.

Ludwig, K. R. (2000). *Isoplot/Ex. Berkeley Geochronology Center, Special Publication* **1a**.

Markl, G. & Bucher, K. (1997). Proterozoic eclogites from the Lofoten islands, northern Norway. *Lithos* **42**, 15–35.

Messiga, B., Tribuzio, R. & Vannucci, R. (1990). Mafic and ultramafic pods with eclogitic relics from the Proterozoic Nagssugtoqidian mobile belt of East Greenland. *Lithos* **25**, 101–118.

Mezger, K. & Krogstad, E. J. (1997). Interpretation of discordant U–Pb zircon ages: an evaluation. *Journal of Metamorphic Geology* **15**, 127–140.

Moecher, D. P., Essene, J. & Anovitz, L. M. (1988). Calibration and application of clinopyroxene–garnet–plagioclase–quartz geobarometers. *Contributions to Mineralogy and Petrology* **100**, 92–106.

Montel, J.-M., Kornprobst, J. & Vielzeuf, D. (2000). Preservation of old U–Th–Pb ages in shielded monazite: example from the Beni Bousera Hercynian kinzigites (Morocco). *Journal of Metamorphic Geology* **18**, 335–342.

Moores, E. M. (1991). Southwest U.S.–East Antarctic (SWEAT) connection: a hypothesis. *Geology* **19**, 425–428.

Newton, R. C. & Perkins, D. I. (1982). Thermodynamic calibration of geobarometers based on the assemblages garnet–plagioclase–orthopyroxene (clinopyroxene)–quartz. *American Mineralogist* **67**, 203–222.

Pattison, D. & Newton, R. C. (1989). Reversed experimental calibration of the garnet–clinopyroxene Fe–Mg exchange thermometer. *Contributions to Mineralogy and Petrology* **101**, 87–103.

Paulsson, O. & Austrheim, H. (2003). A geochronological and geochemical study of rocks from Gjelsvikfjella, Dronning Maud Land, Antarctica—implications for Mesoproterozoic correlations and assembly of Gondwana. *Precambrian Research* **125**, 113–138.

Powell, R. & Holland, T. (1994). Optimal geothermometry and geobarometry. *American Mineralogist* **79**, 120–133.

Powell, R., Holland, T. & Worley, B. (1998). Calculating phase diagrams involving solid solutions via non-linear equations, with examples using THERMOCALC. *Journal of Metamorphic Geology* **16**, 577–588.

Roberts, M. P. & Finger, F. (1997). Do U–Pb zircon ages from granulites reflect peak metamorphic conditions? *Geology* **25**, 319–322.

Seydoux-Guillame, A. M., Paquette, J. L., Wiedenbeck, M., Montel, J. M. & Heinrich, W. (2001). Experimental resetting of the U–Th–Pb system in monazite. In: Altherr, R. (ed.) *79. Jahrestagung der Deutschen Mineralogischen Gesellschaft, 9–14 September 2001. European Journal of Mineralogy, Beiheft*, 172 pp.

Shackleton, R. M. (1996). The final collision zone between East and West Gondwana: where is it? *Journal of African Earth Sciences* **23**, 271–287.

Shiraishi, K., Ellis, D. J., Hiroi, Y., Fanning, C. M., Motoyoshi, Y. & Nakai, Y. (1994). Cambrian orogenic belt in East Antarctica and Sri Lanka: implications for Gondwana assembly. *Journal of Geology* **102**, 47–65.

Steiger, R. H. & Jäger, E. (1977). Subcommission on geochronology: convention on the use of decay constants in geo- and cosmochronology. *Earth and Planetary Science Letters* **36**, 359–362.

Sun, S. & McDonough, W. F. (1989). Chemical and isotopic systematics of ocean basalts: implications for mantle composition and processes. In: Saunders, A. D. & Norry, M. J. (eds) *Magmatism in the Ocean Basins. Geological Society, London, Special Publications* **42**, 313–345.

Talarico, F., Kleinschmidt, G. & Henjes-Kunst, F. (1999). An ophiolitic complex in the northern Shackleton Range, Antarctica. *Terra Antartica* **6**(3/4), 293–315.

Vavra, G. (1990). On the kinematics of zircon growth and its petrogenetic significance: a cathodoluminescence study. *Contributions to Mineralogy and Petrology* **106**, 90–99.

Von Blanckenburg, F., Villa, I. M., Baur, H., Morteani, G. & Steiger, R. H. (1989). Time calibration of a *PT*-path from the Western Tauern Window, Eastern Alps: the problem of closure temperatures. *Contributions to Mineralogy and Petrology* **101**, 1–11.

White, R. W., Powell, R. & Holland, T. J. B. (2001). Calculation of partial melting equilibria in the system $Na_2O–CaO–K_2O–FeO–MgO–Al_2O_3–SiO_2–H_2O$ (NCKFMASH). *Journal of Metamorphic Geology* **19**, 139–153.

Williams, I. S. (1998). U–Th–Pb geochronology by ion microprobe. In: McKibben, M. A., Shanks, W. C., III & Ridley, W. I. (eds) *Applications of Microanalytical Techniques to Understanding Mineralising Processes. Society of Economic Geologists, Reviews in Economic Geology* **7**, 1–35.

Williams, I. S. & Claesson, S. (1987). Isotopic evidence for the Precambrian provenance and Caledonian metamorphism of high grade paragneisses from the Seve Nappes, Scandinavian Caledonides. II. Ion microprobe zircon U–Th–Pb. *Contributions to Mineralogy and Petrology* **97**, 205–217.

Williams, I. S., Buick, I. S. & Cartwright, I. (1996). An extended episode of early Mesoproterozoic fluid flow in the Reynolds Range, central Australia. *Journal of Metamorphic Geology* **14**, 29–47.